The turbulent structure and diurnal growth of the Saharan atmospheric boundary layer

L. Garcia-Carreras[1], D.J. Parker[2], J.H. Marsham[2], P.D. Rosenberg[2], I.M. Brooks[2], A.P. Lock[3], F. Marenco[3], J.B. McQuaid[2], M. Hobby[4]

[1] Department of Meteorology and the Bert Bolin Centre for Climate Research, Stockholm University, Stockholm, Sweden.

[2] Institute for Climate and Atmospheric Sciences, University of Leeds, Leeds, U.K.

[3] UK Met Office, Exeter, U.K.

[4] National Centre for Atmospheric Science, University of Leeds, Leeds, U.K.

Corresponding author: L. Garcia-Carreras (luis.garciacarreras@misu.su.se)

ABSTRACT

The turbulent structure and growth of the remote Saharan atmospheric boundary layer (ABL) is described with *in situ* radiosonde and aircraft measurements and a large-eddy simulation model. A month of radiosonde data from June 2011 provides a mean profile of the midday Saharan ABL, which is characterized by a well-mixed convective boundary layer, capped by a small temperature inversion (<1 K) and a deep, near-neutral residual layer. The boundary layer depth varies by up to 100% over horizontal distances of a few kilometres due to turbulent processes alone. The distinctive vertical structure also leads to unique boundary-layer processes, such as detrainment of the warmest plumes across the weak temperature inversion, which slows down the warming and growth of the convective boundary layer. As the boundary layer grows, overshooting plumes can also entrain free-

tropospheric air into the residual layer, forming a second entrainment zone which acts to maintain the inversion above the convective boundary layer, thus slowing down boundary-layer growth further. A single column model is unable to accurately reproduce the evolution of the Saharan boundary layer, highlighting the difficulty of representing such processes in large-scale models. These boundary-layer processes are special to the Sahara, and possibly hot, dry, desert environments in general, and have implications for the large-scale structure of the Saharan heat low. The growth of the boundary layer influences the vertical redistribution of moisture and dust, and the spatial coverage and duration of clouds, with large-scale dynamical and radiative implications.

1. Introduction

The Saharan atmosphere is a key component of the climate system. Intense solar heating during the boreal summer leads to the formation of a near-surface low pressure system known as the Saharan heat low, which is a major element of the West African monsoon, strengthening the moist, south-westerly monsoon flow from the ocean, as well as the dry Harmattan flow in the north and east (Parker *et al.*, 2005; Lavaysse *et al.*, 2009). The Sahara is also the world's largest source of mineral dust (Prospero *et al.*, 2002; Washington *et al.*, 2003), which has significant implications for both regional and global climate, both via its direct interaction with radiation (Haywood and Boucher, 2000) and its impacts on cloud microphysical processes (Kaufman *et al.*, 2005). The long-range transport and deposition of mineral dust has also been shown to interact with bio-geochemical cycles in remote regions (e.g. Jickells *et al.*, 2005).

The Saharan atmospheric boundary layer (ABL) controls the vertical redistribution and transport of dust, heat, moisture and momentum within the Saharan heat low region

(Cuesta *et al.*, 2009). As a result of the extreme near-surface temperatures, the Saharan ABL commonly reaches 5 – 6 km, making it probably the deepest on Earth (Gamo, 1996). In the morning and early afternoon a small temperature inversion, typically ≤1 K over a depth of around 100 m, separates the Saharan convective boundary layer (CBL) from a deep near-neutral Saharan residual layer (RL), with a lapse rate of approximately 1 K km^{-1}, caused by the previous day's fully developed CBL (Messager *et al.*, 2010). The CBL often reaches its full extent only in the late afternoon (Marsham *et al.*, 2013a), and radiosonde observations show that the RL can sometimes persist over large areas throughout the day (Cuesta *et al*., 2008; Messager *et al*., 2010; Marsham *et al.*, 2013a). This persistence of the RL can be explained by subsidence, either caused by mesoscale circulations induced by albedo variations (Marsham *et al.*, 2008) or larger scale features like the Hoggar mountains in the East (Birch *et al.*, 2012), which suppresses the CBL growth. Air from the Atlantic advected into the Sahara can lead to a persistent shallow CBL (Marsham et al 2013a) and Saharan air advected further south into the Sahel also displays similar characteristics to the Saharan RL (Canut *et al.*, 2000). The large depth of the Saharan ABL allows boundary layer clouds to form via adiabatic cooling, despite the dry conditions, and small errors in humidity in models can have substantial impacts on modelled cloud cover, and thus radiation (Flamant *et al*., 2007; Messager *et al.*, 2010; Marsham *et al*. 2013a). It is hypothesised that the small temperature inversion separating the CBL from the RL means that small perturbations in CBL temperature can have a large impact on vertical mixing, and that they also induce thermally driven circulations that affect the CBL at the mesoscale (Marsham *et al.*, 2008). Modelling studies provide some evidence to support these ideas (Huang *et al*., 2010; Birch *et al*., 2012). There is some evidence that the diurnal cycle in BL-drag on winds at these levels results in an "upper Saharan BL jet" during the morning, analogous to the well-known

nocturnal low-level jet (Marsham *et al.*, 2013a), which affects synoptic-scale transport. The growth of the CBL leads to the breakdown of the nocturnal low-level jet, by entraining and mixing down the high-momentum air, thus producing a rapid increase in near-surface wind speeds and dust emission in the morning (Fiedler *et al*., 2013). There is also evidence from ground-based data that, similarly to the low-level jet breakdown, the downward mixing of the upper Saharan BL winds also causes an afternoon maximum in dust emission (Todd *et al.*, 2013).

Despite the importance of the Sahara for the climate system, routine observations are sparse and the few data that exist are mostly from the periphery of the desert, thus missing the centre of the heat low. This leads to large disagreements between analyses (Marsham *et al.*, 2011), significant biases in operational (Agusti-Panareda *et al.*, 2010; Garcia-Carreras *et al.*, 2013) and climate models (Roehrig *et al.*, 2013), and fundamentally limits our process-based understanding of the Saharan heat low. The subtle vertical structure of the Saharan boundary layer, in particular the residual layer, provides additional challenges for boundary layer parameterisations (Couvreux *et al.*, 2014). The Fennec project is a large-scale, international observational and modelling programme which aimed to produce the most comprehensive dataset of the central Saharan atmosphere to date (Washington *et al*., 2012). The observational programme included two ground-based supersites, one of which was located at Bordj Badji Mokhtar (BBM), Southern Algeria, close to the climatological location of the Saharan heat low (Marsham *et al*., 2013a), with the other supersite further west (Todd *et al*., 2013). Two aircraft campaigns also took place during June 2011 and 2012 from a base in Fuerteventura (Ryder *et al.*, 2013); these included the first-ever flights to sample the vertical structure of the Saharan ABL using an extensive suite of on-board instrumentation.

In this study we aim to describe the characteristics of a typical Saharan ABL, particularly the turbulent and vertical mixing between its various layers and its diurnal evolution. We use a combination of large-eddy modelling and the unique radiosonde and aircraft observations taken in the central Sahara during Fennec, which are described in Section 2. A climatology of the radiosonde data is used to describe the mean structure of the Saharan ABL in Section 3.1, providing the context for the subsequent detailed analysis. Limitations in the aircraft data, described in Section 2.1, make their interpretation difficult. For this reason, the large-eddy simulation results are used in Section 3.2 to investigate the variability of the Saharan ABL, and the key processes governing its diurnal evolution, while in Section 3.3 aircraft data are used to provide supporting evidence for the specific processes described in the model. A single column model version of the Met Office Unified Model is used to evaluate the ability of large-scale models to represent the Saharan ABL in Section 3.4, before summarising the results in Section 4.

2. Method

2.1 Observations

We use radiosondes and eddy covariance estimates of surface fluxes from Fennec supersite-1 at BBM in the central Sahara (star in Figure 1, with solar noon at 1157 UTC on 15 June) to initialise, force and compare with the Met Office Large Eddy Model (LEM) simulation. Vaisala RS92 radiosondes were launched at 3 to 6-hour intervals during 8 – 30 June 2011, providing the first continuous *in situ* measurements of the vertical structure of the remote Saharan atmosphere close to the climatological location of the Saharan heat low (indicated by the 'L' in Figure 1). Conditions were generally moister and drier after 18 June, but there was no clear seasonal variation in the Saharan ABL structure during this period (Marsham *et*

120 *al.*, 2013a provides a comprehensive review of the supersite and the conditions throughout
121 this month). The measurements were used to construct mean profiles of the Saharan ABL at
122 BBM to show to what extent the modelling results represent recurrent features in the
123 observations. A 0900 UTC profile from 20 June 2011 was used to initialise the LEM (Section
124 2.2). This day was chosen because the midday temperature profile was representative of a
125 typical Saharan ABL and the CBL grew to a height of 500 mb by the end of the day, with little
126 influence from synoptic processes.
127 Aircraft measurements from a flight that took place between 1300 and 1515 UTC on 12 June
128 2012 over northern Mali are used to compare with the modelling results (flight B705, white
129 line in Figure 1, see Ryder *et al.*, 2013, for more details on the aircraft campaign). Data used
130 include temperature and three-dimensional wind observations at 32 Hz. A Leosphere
131 ALS450 elastic backscatter lidar with daytime capability was used on board the aircraft. The
132 lidar was pointing at nadir, and had an operational wavelength of 355 nm and overlap range
133 of 300 m. The data used have a vertical resolution of 225 m and an integration time of 20 s;
134 at typical aircraft speeds, the latter translates into a ~3 km footprint. The flight took the
135 form of straight, stacked legs of ~60 km in length – long enough for fluxes to be calculated
136 with the eddy covariance method. By their very nature, the measurements are limited, both
137 spatially and temporally, and complicated by the heterogeneous conditions along the flight-
138 track as well as the simultaneous time and height evolution of the boundary layer while
139 performing the stacked legs. However, these data provide unprecedented detail of the
140 turbulent characteristics of the Saharan ABL and can be used to validate the processes
141 identified with the model.
142

2.2 Large-eddy simulation model

We use Version 2.4 of the Met Office Large Eddy Model (LEM; Gray *et al.*, 2001), a state-of-the-art model for large-eddy simulation and cloud-resolving modelling, to identify and describe the primary processes that control the vertical structure and turbulent mixing processes in the Saharan ABL. The LEM is a nonhydrostatic model with a Boussinesq equation set, using a k-closure and a 3D turbulence scheme. A 30x30x8 km domain with periodic lateral boundary conditions was used with a horizontal grid spacing of 60 m and a variable vertical grid spacing of 11 to 60 m, with highest resolution within the boundary layer and at the residual-layer top, where shear-induced mixing could be important. The resolution is slightly coarser than that typically used to study boundary-layer turbulence – the large depth of the Saharan ABL means that a large domain is needed, limiting the resolution at which the model can be run. The turbulent length scales will, however, scale accordingly, so that a coarser resolution is adequate. A layer damping the prognostic variables to their horizontal means was applied above 7500 m to reduce the reflection of gravity waves from the upper boundary. The model was run from 0900 to 1800 UTC, initialized with a radiosounding launched at 0900 UTC on 20 June 2011 from Fennec supersite-1 at BBM. The time-varying surface sensible heat fluxes were prescribed with a diurnal cycle of eddy-covariance measurements taken at BBM for the same day, smoothed with a 1-hour running mean. A passive tracer was initialized at the start of the run as a spatially homogeneous layer at the lowest model level in order to better visualize the mixing and transport in the CBL, as well as acting as a proxy for boundary layer aerosol such as dust. The model is run with both the radiation and microphysics schemes turned off and without any large-scale forcing, such as large-scale subsidence in relation to the descending motion of the Hadley cell. The objective of the simulation is not to reproduce this particular

day at BBM, but to describe the general characteristics and day-time evolution of a typical Saharan ABL.

2.3 Single Column Model Simulation

In order to evaluate the ability of large-scale models to represent the evolution of the Saharan ABL, the Met Office Unified Model (Walters et al, 2013) was run as a single column model (SCM) with the same initial conditions and surface fluxes as the LEM (see Section 2.2). Radiation was switched off (as in the LEM) so that only the boundary-layer parameterization (Brown et al, 2008) was actually used. Although the cloud and cumulus convection parameterizations were switched on, no clouds were formed during the simulation, so these parameterisations were never triggered. The boundary-layer parameterisation is a first-order turbulence closure where, for unstable boundary layers, the diffusion coefficients are specified functions of height within the boundary layer, related to the strength of the turbulence. There are additional parameterized non-local flux profiles of heat and momentum that have the effect of generating more vertically uniform potential temperature and wind profiles in convective boundary layers. The existence and depth of unstable layers is diagnosed by lifting a moist adiabatic parcel to its level of neutral buoyancy. Mixing across the top of the boundary layer is through an explicit entrainment parameterisation dependent in the simulations here on the surface buoyancy flux, friction velocity and inversion strength (Lock et al, 2000). For stable boundary layers and in the free troposphere, a local Richardson number dependent scheme is used (Brown et al, 2008).

The SCM was run with two different timesteps; 15 minutes, representing a typical operational value, and 1 minute. The vertical grid from the operational global configurations is used, which has 62 levels below 40km with the spacing increasing quadratically with

height above the surface, to give a spacing of around 300 m at 3 km. Two finer grids are also tested, both with a 1 minute timestep. The finest grid has 140 levels with a spacing of 90 m at 3 km and the intermediate grid has 70 levels with a spacing of 200 m at 3 km.

3 Results

3.1 Mean Saharan ABL vertical profile observed at Fennec supersite-1

Figure 2a shows the mean atmospheric profile over BBM for 23 radiosondes launched at 1200 UTC (11:45 local time) during June 2011. Each profile was normalized to its own CBL and RL depths, then rescaled to the mean of all CBL and RL depths (820±80 mb and 550±50 mb respectively) before averaging all the profiles to construct a mean profile of the Saharan ABL (Figure 2). The CBL and RL heights were determined subjectively, by identifying temperature inversions, coincident with consistent changes in humidity and winds. Only the midday profile is shown as radiosondes on all days were only available at 6-hourly intervals, and profiles at dawn and dusk are complicated by the transition from day-time to night-time conditions. The modelling results in Section 3.2 also show that the general structure of the profile in Figure 2 persists throughout most of the afternoon.

There are a number of features of the Saharan ABL which set it apart from a typical boundary layer. At 1200 UTC, before the CBL has time to fully develop, the Saharan ABL is made up of an actively-growing CBL, driven by high sensible heating at the surface, capped by a very weak inversion (often ≤ 1 K over 10 – 20 mb in height), with a deep, near-neutral RL above it, produced by the previous day's CBL. The rapid change in wind direction between the CBL and RL is consistent with these two layers being decoupled, despite the small temperature inversion separating them, with the RL winds aligning more closely with the free-tropospheric winds above. The weak stability observed in the RL can be explained

by the presence of shear at the RL top, which will transport warm, free-tropospheric air downwards, although radiative effects from dust and water vapour have also been suggested as contributing factors (Cuesta *et al.*, 2009). The mean lapse rate in the RL was 1 K Km^{-1}, although this value was frequently lower, as a small number of cases with a more stable profile above the inversion dominate the average. This structure is consistent with past observations of the Saharan boundary layer (Messager *et al.*, 2010). The presence of such a weak capping inversion is expected to make the evolution of the Saharan ABL hard to represent in global models, as the ABL will likely be sensitive to the surface fluxes and vertical resolution of the model. The RL typically reaches heights of 550 mb. Despite the strong sensible heating at the surface, the CBL typically erodes the temperature inversion completely only by late afternoon, and in some cases does not reach the top of the RL at all (Cuesta *et al*., 2008; Messager *et al*., 2010; Marsham *et al.*, 2013a).

The presence of a weak inversion and a near-neutral residual layer both reduce the return force on overshooting parcels from the CBL relative to the usual case of a CBL capped by a stratified troposphere. Assuming no entrainment, the distance travelled by an overshooting plume, *h*, can be estimated theoretically by considering (very simply) the transfer of kinetic to potential energy:

$$h = \frac{w^2}{2g(\frac{T}{T_0} - 1)} \quad (1)$$

where *w* is the vertical velocity of the plume at the temperature inversion, *T* and T_0 are the temperatures of the parcel and environment respectively and *g* is gravitational acceleration. For a 10 m s^{-1} updraught with a 0.5 K temperature deficit, which represents the most extreme case in the aircraft observations, the overshooting distance is 3300 m. This is likely to represent an upper bound, as many updraughts are weaker, the inversion can be

stronger and the RL is often slightly stable. Entrainment into the plume will reduce its temperature difference from the environment, but also reduce its momentum. This simple calculation, however, does show that it is feasible for parcels to travel far into the residual layer, as hypothesized in Huang *et al.* (2010), without the need for particularly hot plumes in the CBL.

The large distance travelled by overshooting parcels within a near-neutral layer raises the possibility that turbulence in the CBL may induce vertically-extensive mixing in the RL, or even lead to detrainment from the CBL top into the RL akin to cumulus detrainment, albeit without the presence of diabatic warming. This would be a unique feature of the Saharan ABL (or perhaps deep, dry desert boundary layers in general), and has implications for the diurnal evolution of the CBL, as well as the vertical, and subsequent horizontal long-range, transport of recently uplifted dust.

The gradient Richardson number, *Ri*, is a dimensionless quantity representing the ratio between shear and buoyant forcing and is a measure of the instability in the atmosphere :

$$Ri = \frac{\frac{g}{T_v}\frac{\partial \theta_v}{\partial z}}{(\frac{\partial U}{\partial z})^2 + (\frac{\partial V}{\partial z})^2}, \qquad (2)$$

where ϑ_v is virtual potential temperature, T_v is virtual absolute temperature, z is height and (U,V) are the zonal and meridional wind components. Where $Ri < 0$ the atmosphere is convectively unstable, while where $0 < Ri < 0.25$ the atmosphere is turbulent due to mechanical generation by shear. Where $Ri > 1$ the atmosphere is not turbulent. The values in between ($0.25 < Ri < 1$) represent a regime where the atmosphere maintains its current state, be it laminar or turbulent. This is due to the fact that laminar flow becomes turbulent when $Ri < 0.25$, but turbulent flow becomes laminar when $Ri > 1$, producing a hysteresis

effect (Galperin *et al.*, 2007; Stull, 1988). Figure 2b shows boxplots of the gradient Richardson number in each layer for all the 1200 UTC BBM radiosondes. In the CBL, the atmosphere is turbulent (Ri < 0.25) on most days. The free troposphere, on the other hand, is almost never unstable, and has Ri > 1 on most days. Conditions in the RL are more complex. Shear-induced turbulence is significant, particularly close to the RL top (30% of days with 0 < Ri < 0.25), while the largest proportion of days have 0.25 < Ri < 1, where turbulent mixing is not generated, but can be maintained. Radiosonde wind profiles show that wind shear is a recurrent feature both at the CBL and RL tops, and may therefore be a significant contributor to turbulence and mixing in, and between, both layers (not shown).

3.2 Large-eddy modelling of the Saharan ABL

3.2.1 Validation of the Saharan ABL structure in the Large Eddy Model simulation

The evolution of the Saharan ABL in the LEM can be compared to radiosonde data for the same day used for the initialization. The idealized modelling approach means that an exact match is not expected, particularly because in the LEM the extent of CBL development is controlled solely by the initial profile and surface fluxes, with no impacts from external factors or some missing processes (discussed below). It is important, however, to determine whether the LEM is representative of reality, despite these deficits.

Overall, the model can reproduce the general Saharan ABL structure and its diurnal evolution (Figure 3). At 0900 UTC, when the model is initialized, the nocturnal inversion reaches 900 mb (not shown). By 1200 UTC this inversion is eroded in both the model and observations, but the LEM CBL grows more slowly throughout the day, reaching 850 mb (750 mb in the observations) at 1200 UTC, and 620 mb as opposed to 580 mb at BBM at

1500 UTC. In terms of CBL temperatures, the model initially warms faster, but is cooler than observations at the end of the day, although differences are generally less than 0.5 K, reaching a maximum of 1 K at 1800 UTC. The RL is moister than the CBL, which allows the CBL humidity to increase as it grows between 1200 and 1500 UTC. The final CBL humidity of 4 kg kg^{-1} is consistent between the runs, suggesting there is no large-scale moisture advection during the day. These differences, however, are not expected to have a significant impact on the CBL processes, as the general structure of the Saharan ABL, with a CBL and near-neutral RL separated by a small inversion are well characterized, and representative of the average Saharan ABL profile (Figure 2a).

The three main mechanisms that the LEM is not representing are large-scale advection, large-scale subsidence and the impact of dust on the radiation budget. The aerosol optical depth on 20 June 2011 was ~1, as derived from the Cimel sun-photometer at BBM (Marsham *et al.*, 2013a). Dust interacts with both longwave and shortwave radiation, and can contribute to atmospheric heating in the order of a few K day^{-1}, while decreasing surface temperatures, although exact heating rates are uncertain and depend on the particle size distribution (Ryder *et al.*, 2013). Depending on whether the dust is located in the CBL or RL, this would help destabilize or stabilize the CBL respectively. Although radiative effects from dust are likely to be dynamically important, their potential impacts on the Saharan ABL are so wide-ranging, that they are beyond the scope of this paper. Large-scale advection of the RL can affect the stability of the CBL. The RL will also be fairly variable in the horizontal (given that the CBL height is variable), so advection at the RL top could contribute to the changes at BBM between 15 and 18 UTC at the top of the RL. Changes at the top of the RL due to advection are not represented in the LEM, but given that at the top of the RL there is usually a strong inversion (e.g. Figure 2a) changes in its height during the day should not

affect the turbulent processes below. Finally, large-scale subsidence induces upper-level warming, and is likely to also have an impact on the Saharan ABL structure.

3.2.2 Mean CBL and RL properties

Figure 4 shows the diurnal evolution and horizontal variability of the Saharan ABL in the LEM during the time of quickest CBL growth. Although the surface fluxes and initialization (including the surface tracer) are horizontally homogeneous, there is substantial variability in the CBL depth and tracer concentrations at the horizontal turbulent eddy scale (1 – 2 times the CBL depth, consistent with the spacing in up and downdraughts, Figure 4, right panels). Even at 1300 UTC, when the CBL is still relatively shallow, changes in CBL depth of ~100 mb (~1 km) can be observed over short distances (e.g. between x = 10 and 12 km, Figure 4a). By 1600 UTC this variability has increased to >200 mb (~2.3 km, Figure 4g). Horizontal variability in CBL height due to turbulence is not surprising, and this would be expected to scale with the CBL height, which in this case is large. However, as discussed in Section 3.1, the small temperature difference between the CBL and RL, combined with the weak stability within the RL also play an important role, as overshooting parcels will travel further than in a boundary layer with a stronger inversion and stronger RL stability. Evidence for this is also found in the aircraft measurements, where an overshooting plume is observed within the RL rising at 6 m s^{-1} despite being at least 60 mb above the CBL top (Figure 5, with the plume centred at 1.8 km, see Section 3.3 for a full discussion on the CBL evolution in the aircraft data). The plume is only 0.5 K cooler than the RL, therefore there is only a very weak buoyancy force that needs to overcome the high initial upward momentum, and the plume temperatures and vertical velocities are consistent with the model (e.g. Figure 4b, x = 9km or Figure 4f, x = 0 km, potential temperatures not shown).

Within the CBL, entrained air from the RL can be carried down nearly undiluted all the way to the surface (not shown, although Figure 4e shows a plume of only partially diluted entrained air descending as far as 900 mb at x = 10 km). As the CBL is continuously growing, thus constantly entraining clean air, the tracer is never well mixed within the CBL, leading to significant horizontal variability in tracer concentrations (Figure 4, left panels). The large horizontal variability in the model, which has spatially-homogeneous surface boundary conditions, shows the extent to which a single atmospheric profile, for example from radiosonde observations, can differ from the average over an area the size of an NWP grid box (an issue which is also discussed for shallower boundary layers in the USA in Weckwerth *et al.*, 1996). The interpretation of dust measurements must also take into account the large variability in concentrations that can occur solely by turbulent processes.

CBL variability also controls the formation of clouds. Despite the extremely dry conditions, the large depth of the Saharan ABL means that parcels can still ascend to their lifting condensation level, forming boundary layer clouds, even at around 5 km altitude (Parker *et al.*, 2005). For example, at 1600 UTC, when the CBL has reached its maximum extent, clouds form where the CBL is locally deepest (x = −9 km, Figure 4g and h). By 1700 UTC, cloud cover in the model reaches a maximum value of 4%, consistent with, although on the lower end of, a climatology based on satellite observations (Stein *et al.*, 2011). The conditions in the model here are somewhat drier than the average (c.f. Figure 2 and Figure 3), and the maximum CBL top can be higher than in the LEM simulation, where it reaches 600 mb, which would enable more parcels to reach their lifting condensation level, thus increasing cloud cover. Failure of large-scale models to correctly represent the Saharan ABL will not only affect cloud fractions, but also the timing and duration of Saharan clouds, which affects the radiative budget in the Sahara. Dust and moisture are often associated in the central

Sahara (Marsham *et al*., 2013a), so errors arising from dust and cloud are likely to be coupled. The small depth of these clouds (~20mb), much less than a typical NWP vertical grid spacing, coupled with their sensitivity to CBL humidity and the Saharan ABL evolution means that the representation of Saharan clouds in global models is likely to be poor, but the extent of this error and any radiative bias associated with it is currently poorly understood.

One effect of the weak temperature inversion is that CBL plumes are only marginally cooler, sometimes even warmer, than the RL. This allows transport from the CBL to the RL, as plumes can detrain at the CBL top. Although the local CBL top, indicated by the strongest gradient in tracer concentration, can be identified by the transition from the warmer colours to blue in Figure 4 (left panels), consistent with the vertical velocities (Figure 4, right panels) and potential temperatures (not shown), significant tracer concentrations can be found above the CBL top in regions where the CBL is locally shallow, for example between x = −3 and 0 km at 1600 UTC. Low concentrations of tracer can also be observed above the deepest CBL tops, for example at x = 5 km and 580 mb in height at 1500 UTC (in slightly lighter blue than the background) and more such events can be observed in animations of the 2D tracer evolution. Tracer concentrations in these plumes are low due to the fact that air is being detrained into a deep, tracer-free RL, and the presence of mixing within the RL quickly dilutes the detrained parcels. Although the impact of detrained plumes on tracer transport is small, their thermodynamic impact, particularly in terms of CBL growth, may be important.

Figure 6 shows probability density functions of potential temperature and vertical velocity anomalies in the CBL and RL. Different methods were used to derive these anomalies in the different datasets, due to differences in the information available. For the LEM, the 3D field

was used at 1400 UTC, with the anomalies representing deviations from the horizontal domain mean at each height. Only data above 900 mb were used, to only include the well-mixed portion of the CBL. Tracer concentrations were used to differentiate between the CBL and RL in the LEM data to account for the horizontal variability in CBL height, which is not captured in the other datasets. A test using only the mean CBL height to differentiate the layers in the LEM did not significantly alter the distribution. For the 1200 UTC BBM radiosondes no vertical velocity data were available, and the temperature anomalies were computed as perturbations from the detrended profile, to remove the slight stability of the RL and only show the turbulent variability in the data. Finally, the bottom three runs of the aircraft data (960 – 730 mb, 1352 – 1434 UTC) were used for the CBL, and the western end of the top two runs for the RL (680 – 620 mb, 1455 – 1514 UTC), and the anomalies were computed by high-pass filtering the time series with a 10 km cut-off length scale (see Section 3.3.1 for more details on the aircraft path). This removed the impact of any mesoscale variability along the flight track.

Despite the strong surface heating, the distribution of temperatures in the CBL is very narrow, mostly confined to ±0.5 K in all datasets. While the BBM radiosonde data show a slightly broader distribution, this could be accounted for by slight changes in stability within the RL unaccounted for when detrending the profile. The narrow temperature distribution can be explained by the fact that, due to the small temperature difference between the CBL and RL, entrained air will only be slightly warmer than the CBL air. Eddies due to strong surface heating are also quickly mixed into a very deep CBL, reducing their impact. Finally, detrainment of the hottest plumes from the CBL top will also act to reduce the temperature range within the CBL.

The vertical velocities, on the other hand, are mostly confined to −5 to 5 m s^{-1} for the CBL as a whole, although peak vertical velocities are higher on average close to the CBL top, reaching up to 10 m s^{-1} in the aircraft observations. Again, despite the differences in how the anomalies are computed, the match between the model and aircraft observations is very close, confirming that the model is representing the turbulent characteristics of the Saharan ABL in an appropriate manner.

The RL distribution in temperatures is also relatively narrow. This suggests some degree of mixing within the RL. The presence of significant vertical velocities throughout the RL (±2 m s^{-1}) is consistent with both turbulent mixing and the presence of waves, and results in Section 3.2.3 show evidence for both processes having a contribution. These vertical velocities are not simply a result of sampling overshooting plumes within an otherwise stable RL, as this would lead to a more discontinuous distribution, with many low vertical velocity events and a few high velocity events. Furthermore, the sampling of the LEM data effectively eliminates overshooting plumes from the distribution. Turbulence in the RL helps maintain the near-neutral state of the layer and could contribute to CBL detrainment, by mixing overshooting plumes into the rest of the RL, preventing them from returning to the CBL.

3.2.3 Diurnal Evolution of the CBL and RL

The diurnal evolution and growth of the CBL is important to understand the characteristics of the Saharan heat low. The growth of the CBL into the RL controls the vertical, and subsequent long-range horizontal, transport of heat, moisture and mineral dust. Clouds are also a recurrent, albeit poorly understood, feature in the Sahara, and depend critically on

426 the Saharan ABL growing deep enough to reach the lifting condensation level of such a dry
427 atmosphere.
428 Figure 7 shows profiles of modelled potential temperature profiles and fluxes. Figures 7a,b
429 show the "classic" BL flux profile of a warming CBL with fluxes decreasing to a minimum at
430 CBL top, above which the atmosphere is cooling due to entrainment. At 1200 and 1300 UTC
431 the CBL is growing into a moist RL and the CBL has negative fluxes of humidity and is
432 moistening, with drying of the RL above. By 1600 UTC the CBL is growing into the dry FT and
433 has positive fluxes of humidity and is drying. At the intermediate times of 1400 and 1500
434 UTC the flux profile is more complex with two clear minima in the heat flux at 1400 UTC. We
435 discuss this evolution and the processes responsible in this section.
436 The combination of a weak temperature inversion, deep near-neutral RL and strong sensible
437 heating at the surface should all contribute to a rapid growth of the CBL. In the LEM
438 simulation, however, the CBL completely erodes the RL only by 1600 UTC (Figure 7e).
439 Idealised theoretical studies suggest a constant ratio between the entrainment and surface
440 buoyancy flux. More realistic laboratory and large-eddy simulation studies have found the
441 ratio to vary between about 0.1 and 0.2 (Deardorff *et al*., 1980; Sullivan *et al*., 1998; Brooks
442 and Fowler, 2007), and that the ratio increases with wind shear across the inversion (Moeng
443 and Sullivan, 1994; Pino *et al.*, 2003; Conzemius and Fedorovich, 2006). Here we find this
444 flux ratio (the ratio between surface fluxes and the minimum in fluxes, found in the
445 entrainment zone) to be substantially smaller than in previous studies, just 0.03, despite the
446 presence of shear at the CBL top, and this reduced entrainment flux is linked to the slow
447 growth of the CBL (Figure 7a-b). The flux ratio increases throughout the afternoon, only
448 approaching 0.2, the value typically used by entrainment rate closures in general circulation
449 models, at 1730 UTC (c.f. Figure 13 in Section 3.4). At this time the CBL has eroded all of the

RL, and is therefore capped by the stable, free troposphere, suggesting that the weak entrainment fluxes are associated with the particular structure of the midday Saharan ABL.

Although the CBL deepens via entrainment throughout the day, detrainment of some of the plumes that overshoot into the RL, as shown in Section 3.2.2, reduces the entrainment rate, slowing the rate of growth. Under strongly convective conditions entrainment typically proceeds via the overshooting of plumes into the inversion or overlying warmer air where they become negatively buoyant and sink back into the boundary layer, bringing some of the overlying air down with them (Sullivan et al. 1998). Here the inversion is weak and the overlying air only slightly warmer than that in the CBL. The small temperature difference means that convective plumes penetrating into the RL experience little negative buoyancy, even if cooler than the RL air; they may thus penetrate a significant distance, while shear induced turbulence at the edge of the plume or existing turbulence in the RL may detrain some air from the plume into the RL before it sinks back into the CBL. Some plumes may be warmer than the RL air; these remain positively buoyant in the RL and do not sink back into the CBL. These plumes thus act to remove material from the CBL, reducing the rate of growth by entrainment. They transfer the warmest parcels of air from the CBL to the RL, acting to reduce the rate of warming of the CBL and to heat the RL; this constitutes a positive heat and buoyancy flux contribution at the top of the CBL, reducing the magnitude of the negative entrainment flux between the two layers. This process acts to maintain the temperature differential between the two layers against the warming of the CBL, reducing the rate at which the inversion is eroded and slowing CBL growth further.

As the CBL grows, overshooting plumes begin to reach the RL top. These can be identified as parcels of nearly undiluted tracer concentrations with associated negative temperature anomalies extending up to 600 mb in height (e.g. at x = 7 km in Figure 9b). These plumes

entrain warm, dry free-tropospheric air into the RL, thus increasing CBL detrainment (as the parcel will no longer be negatively buoyant) and also producing a negative heat flux and positive moisture flux at the RL top. This gives rise to the two entrainment zones with two minima in heat fluxes at 1400 UTC (Figure 7c).The lower zone is where the CBL is growing into the moist RL. The upper zone is in a slightly drier and more stable portion of the RL (650 to 570 hPa). The warming of the RL due to entrainment at the RL top (620 hPa) helps maintain the temperature inversion between the CBL and RL, slowing down CBL growth further. By 1500 UTC there is a single, deep (~150 mb or 2.4 km) region of negative heat fluxes. At this time, however, the CBL has not completely eroded the RL yet, and two mixing regions remain; one between the CBL and the lower RL (600 to 670 hPa), and the other at the RL top (530 to 600 hPa). This is apparent from the moisture flux; at 1200-1300 UTC the moisture flux is negative, as the RL is moister than the CBL (Figure 3), which leads to a downward transport of moisture as the CBL grows. From 1400-1500 UTC moisture fluxes remain negative within the CBL, but become positive above, as dry air is transported downwards at the RL top. This is in contrast with 1600 UTC, when moisture fluxes are positive throughout the CBL and the CBL is growing into the FT, coinciding with an increase in entrainment fluxes, which reach 18% of the surface fluxes at 1730 UTC – this is now consistent with the typical 10%-20% of the surface flux observed by previous studies of entrainment.

At all times, momentum fluxes within the RL are non-zero, demonstrating the presence of turbulent mixing within the RL (Figure 7, dashed lines). At 1200 - 1300 UTC these momentum fluxes are relatively weak, with a peak at the top of the RL. Wave patterns in the potential temperature and vertical velocity can also be observed at the RL top (e.g. at (x,y) = (10,10) and (−5,−3) in Figure 8a and b). The waves are oriented perpendicular to the mean

498 wind and have length scales in the order of a few hundred metres (longer 5-10 km waves
499 can perhaps be seen, but are much clearer in Fig 9a one hour later). These waves are
500 consistent with shear at the RL top, which is a persistent feature of the Saharan ABL (Figure
501 2c), generating the momentum flux at this location. As highlighted in Figure 2b, the
502 conditions in the RL are such that even if turbulence is not generated, it can be maintained;
503 this could potentially allow the impact of shear-induced turbulence to extend downwards.
504 The combination of near-neutral conditions and turbulence, albeit weak, in the RL provide a
505 viable mechanism for the mixing out of overshooting CBL plumes.
506 Later in the afternoon a wave pattern develops in the potential temperature and vertical
507 velocities, which are 90° out of phase (Figure 9a), of larger magnitude and wavelength (in
508 the order of ~5 – 10 km) to the waves observed at 1300 UTC (Figure 8). Plumes that
509 penetrate the RL, without reaching the top (as shown by the tracer concentrations at 665
510 mb, Figure 9a) line up with the cold temperature anomalies aloft, and lie between the
511 positive and negative vertical velocity anomalies (e.g. at x = -1 and 2 km, Figure 9b). This
512 indicates that overshooting plumes also generate waves within the RL. The large spread in
513 vertical velocities in the RL (Figure 6b) can therefore be associated partly with these waves,
514 and partly with the turbulent fluxes in the RL associated with shear-induced mixing and CBL
515 plumes overshooting the RL top. The presence of waves in the RL, and entrainment at the RL
516 top, has also been observed in Lidar measurements over Paris (Fochesatto *et al.*, 2001).
517 In summary, in the afternoon, at the time of most rapid CBL growth, there are two possible
518 fates for rising plumes; the coolest CBL plumes entrain RL air, contributing to CBL warming
519 and growth. The warmest plumes detrain into the RL. This reduces the entrainment flux at
520 the CBL top, contributes to turbulent mixing within the RL and generates waves that
521 increase the variability of potential temperature and vertical velocity at the RL top. Later in

the afternoon, the CBL is deep enough that detrained plumes also warm the RL by entraining free tropospheric air, producing a heat flux profile with two entrainment zones. Overall, this means that while CBL detrainment can only occur due to the presence of a weak temperature inversion, it also acts to maintain the inversion. Weakened entrainment also slows down CBL growth, and may contribute to the Saharan ABL not reaching its maximum extent until late in the afternoon despite the presence of both strong surface heating and a very weak temperature inversion, as found in observations (Figure 2, Cuesta *et al*., 2008; Marsham *et al.*, 2013a).

3.3 Aircraft Observations of the Saharan ABL

3.3.1 Overview of Aircraft Observations

The aircraft case-study took place on 12 June 2012, and aimed to sample the vertical structure of the boundary layer in northern Mali, as close to the Saharan heat low as the aircraft range permitted and where the CBL was forecast to be hot and deep (white line, Figure 1). The east-west track (-5.4 to -4.4°E) was first overflown at high altitude, and two Vaisala RD94 dropsondes were launched at either end (Figure 10, black lines) before descending to minimum safe altitude (~80 m above ground level). During the descent the aircraft travelled eastward to −4°E and 550 mb in height, then turned around comple□ng the descent westward to the western end of the bottom run in Figure 10. The dropsondes were used to identify the heights at which to fly the subsequent legs, so that they would best capture the layers of interest in the Saharan ABL. The dropsondes were launched at 1313 and 1320 UTC, with the stacked legs taking place between 1352 (start of lowest leg) and 1514 UTC (end of the uppermost leg in Figure 10). The aircraft then ascended westward from the western end of the uppermost run.

546 The track was characterized by a synoptic low-level temperature gradient with lower
547 pressures in the east, which is consistent with the albedo gradient along the flight path
548 (decreasing West to East, not shown), although the pressure gradient may also be due to
549 synoptic temperature changes in the heat-low region. The dropsonde profiles are consistent
550 with the low-level temperatures, with a warmer and deeper CBL in the East, reaching 770
551 mb, compared to the West where it reached 820mb, and RL heights of 520 and 540 mb
552 respectively. The temperature difference across the CBL top in both cases was <1 K, but the
553 water vapour mixing ratio and wind profiles (not shown) confirm that this weak lid was
554 acting as a capping inversion. Lidar data were used to estimate the CBL height along the
555 track, by visually inspecting each single lidar profile and subjectively identifying a
556 discontinuity in the gradient of the backscatter with height (stars and dashed line in Figure
557 10). The lidar captures the large variability in CBL depths at the horizontal turbulent eddy
558 scale, with a change of > 100 mb between x = 20 and 25 km, consistent with the LEM. At the
559 mesoscale, the lidar-derived CBL height is consistent with the low-level temperatures,
560 showing deeper boundary layers in the East, with a fairly distinct transition at 60 km
561 (4.9°W).
562 The presence of a transition between two boundary layer heights is confirmed in the *in situ*
563 aircraft measurements taken just under two hours later. The two highest runs (at 680 and
564 620 mb) show mostly laminar conditions for x < 60 km, with low values of $\overline{w'\theta'}$, except for a
565 few bursts in turbulence due to overshooting plumes (for example at x = 40 km, Figure 11b,
566 which is the plume shown in more detail in Figure 5). In the eastern section of the flight
567 track the high values of $\overline{w'\theta'}$ are indicative of active turbulence. These results suggest that,
568 at this time, where x < 60 km (i.e. the eastern section) was within the CBL, while the CBL top
569 in the west was below 680 mb, with the aircraft flying within the RL above this height. The

570 eastern and western portions of the track were therefore considered separately in the rest
571 of the analysis (with the boundary given by the vertical dash-dotted line in Figure 10).
572
573 ### 3.3.2 Saharan ABL structure and evolution as observed in aircraft
574 data
575 Interpretation of the aircraft data is made difficult due to the time evolution of the Saharan
576 ABL throughout the flight. Although the Saharan ABL was sampled at a variety of heights,
577 aimed to capture the CBL and RL, it is, for the most part, impossible to ascertain definitely
578 from the *in situ* data how the different layers evolve during the flight, and so where the
579 aircraft is flying at any given time relative to the CBL and RL tops. Although it is difficult to
580 gain an overarching understanding of the Saharan ABL from the aircraft observations alone,
581 it is possible, however, to find evidence for some of the boundary-layer processes described
582 with the model data.
583 Turbulent fluxes can be computed for each level run from the aircraft data using the eddy-
584 covariance technique. The eastern and western portions of the flight track were considered
585 separately (Figure 12, stars and crosses respectively). On these level runs, anomalies were
586 computed by high-pass filtering the data with a 10 km length scale cutoff, in order to
587 remove any mesoscale variability in the data. The aircraft profiles (descending to minimum
588 altitude and ascending away from the study region, not shown in Figure 10) were at a very
589 shallow angle (2 – 4%), which also allowed the computation of turbulent fluxes as a function
590 of height, in this case using short averaging lengths, as in Brooks *et al.* (2003) (Figure 12,
591 lines). The high-pass filtered profile was used, with a 5-km cutoff, to remove any vertical
592 variability in the data. The averaging of the anomalies to calculate the fluxes was performed
593 with a 10-km running mean (200 – 400 m change in altitude), thus minimizing the effect of

changing altitude on fluxes. On the descent, the east-west boundary (at x = 60 km) was crossed while the aircraft was at 840 mb. The advantage of using the aircraft profiles is that there is little time-evolution between the measurements made at each height within a single profile. For the descent the layers can be identified using the dropsonde data, and at this earlier time the aircraft crosses a large portion of the RL. On the other hand, the shorter averaging length used, compared with the flux calculations performed for the level runs, introduces some noise to the flux estimates and the measurements are affected by horizontal variability in CBL properties, which can be considerable over short distances as can be seen in Figure 10.

The level runs show higher surface heat fluxes in the warmer, eastern portion of the flight-track, leading to a deeper CBL (Figure 12a). The top leg is still within the CBL in the east, but is in the entrainment zone in the west, consistent with what was expected by inspecting the *in-situ* data directly (Figures 10a and b). Although the low-level temperature difference between the two sections is only 1.5 K, there is a large change in surface fluxes from 240 to 330 W m^{-2}. The entrainment zone fluxes are only a small fraction of the surface fluxes (7%), also consistent with the weak entrainment observed in Figure 7, which appears to be a characteristic feature of the Saharan ABL. The heat fluxes near the surface calculated using the downward profile match the fluxes from the level run in the west, providing some validation for the methods used. The magnitude of the profile-fluxes at higher altitudes in the CBL is similar to, but slightly smaller than those calculated with the level runs, consistent with the measurements being taken earlier in the day. Fluxes are positive up to 750 mb, which implies that CBL heights along the descent varied between 850 mb (as seen in the first dropsonde) and just above 750 mb, consistent with the lidar measurements (Figure 10) and the variability in the LEM simulation (e.g. Figure 4a).

618 Momentum fluxes are positive below 550 mb during the aircraft descent, indicating the
619 presence of turbulence within the RL (Figure 12b, solid line). There is a maximum in
620 momentum fluxes at 625 mb. This is lower than the RL top as seen in the dropsondes, but
621 may correspond to the RL top at the aircraft location: at this height the aircraft is flying
622 outside the track shown in Figure 10. The momentum fluxes are consistent with the LEM
623 simulation, which showed shear-induced mixing at the RL top, and there is a weak minimum
624 in sensible heat fluxes of −20 W m^{-2} at the same height. During the ascent out of the study
625 region later in the afternoon, the aircraft crosses a region with negative sensible heat fluxes
626 and a peak in momentum fluxes between 610 to 530 mb, showing the presence of an
627 entrainment zone. The aircraft potential temperature measurements show an inversion at
628 500 mb, and a dropsonde launched slightly later, when the aircraft was flying at 420 mb,
629 also shows a well-mixed CBL up to 520 mb (not shown). This entrainment zone therefore
630 appears to correspond to the CBL top once it has completely eroded the RL. The higher
631 magnitude of the fluxes compared to the level legs, where the CBL is still growing, is
632 consistent with the LEM results (Figure 7), with weak entrainment fluxes while the CBL is
633 capped by a small temperature inversion and a deep RL, while entrainment fluxes increase
634 once the RL is completely eroded and the CBL is capped by the stable free troposphere.
635 Within the RL there is variability in potential temperatures and vertical velocity of similar
636 length scale and magnitude to the waves induced by overshooting plumes described in
637 Figure 9, although the length scale is also consistent with the size of turbulent eddies in the
638 Saharan ABL (Figure 11a and b, western section). Spectral analysis outlined in Matthews and
639 Madden (2000) was used to determine the spectral coherency (which can be considered as
640 the spectral equivalent to the correlation between two data sets) and the phase difference
641 as a function of length scale between potential temperature and vertical velocity. The

642 analysis was applied separately to the western (Figure 11c) and eastern (Figure 11d)
643 sections of the flight track. Within the RL (i.e. in the west) potential temperature and
644 vertical velocity co-vary significantly at scales of 1 – 6 km (Figure 11c), which agrees with the
645 variability observed directly in Figure 11a. As in the LEM (Figure 9), the phase shift between
646 these two quantities in the observations is of ~90° (inset in Figure 11c), consistent with
647 waves, generated by plumes. Within the CBL the presence of these waves is much less clear
648 as turbulent mixing dominates the variability in temperature and winds, although there is a
649 small peak in coherency at 680 mb for length scales above 6 km , with a phase shift of 270°
650 (Figure 11d, solid line).
651 The aircraft observations are consistent overall with the processes described with the model
652 results in Section 3.2. The dropsondes launched between 1300 and 1330 UTC show the
653 same overall structure as the radiosonde data (Figure 2a), with a CBL height of ~800 mb, and
654 a temperature inversion of <1 K. Along part of the flight-track this inversion is not eroded by
655 1500 UTC. Fluxes measured in the entrainment zone were weak, and positive momentum
656 fluxes, as well as waves, were measured throughout the RL, consistent with boundary layer
657 detrainment affecting entrainment and boundary layer growth, as described in Section
658 3.2.3. Once the observed CBL reached the FT entrainment fluxes increased, consistent with
659 the LEM.
660

661 ## 3.4 Representation of the Saharan ABL in larger-scale models

662 In Section 1 we have described the significance of the Saharan ABL for the correct
663 representation of the dynamics and thermodynamics of the large-scale Saharan heat low, as
664 well as the transport of mineral dust. The results in this study highlight the importance of
665 the detailed structure of the Saharan ABL in controlling its variability and diurnal evolution,

in particular small-scale features such as the small temperature inversion, and shear-induced mixing at the RL top. The LEM was run with a high vertical (10 – 35 m below the RL top) and temporal (in the order of seconds) resolution in order to accurately capture these processes. The coarse vertical resolution of operational numerical weather prediction and climate models, particularly at the higher altitudes that the Saharan CBL top can reach, are likely to struggle to capture many of the processes described here. Couvreux et al (2014) simulated the diurnal cycle in the semi-arid region of the Sahel and found that, even with a vertical grid finer that 100 m, their SCM failed to reproduce the fine vertical structure that separated the boundary layer from an overlying layer of Saharan air. Global configurations of the Met Office Unified Model use a timestep from 10 to 20 minutes, depending on horizontal resolution, which may also create problems if the atmospheric profiles change significantly over this time period, for example as a result of the strong surface heating. In order to evaluate the ability of large-scale models to represent the evolution of the Saharan ABL, the Met Office Unified Model was run as an SCM with the same initial conditions and surface fluxes as the LEM. The SCM was run with two different timesteps; 15 minutes, representing a typical operational value, and 1 minute. The vertical grid from the operational global configurations is used, with 62 levels, and two finer grids with 70 and 140 levels were also tested, both with a 1 minute timestep.

Overall the SCM could be argued to perform reasonably well, with temperature differences compared to the LEM simulation less than a few tenths of a degree (Figure 13a,b). Given the surface heat fluxes are specified, however, this is perhaps not too surprising. Interestingly the SCM shows much more sensitivity to timestep with 62 levels (Figure 13a) than it does to vertical resolution at a fixed timestep (Figure 13b). This can also be seen in the time evolution of the CBL depth (Figure 13c), defined as the height of the minimum heat flux for

690 the LEM and the inversion base for the SCM. The jump in CBL height in the LEM at 1430 UTC
691 is due to the merging of the two entrainment zones (as seen in Figure 7c), and so an
692 overestimate of the actual CBL top. The SCM shows too rapid growth during the morning,
693 especially early on with the shorter timestep, and by 1400 UTC leads to a CBL that is too
694 deep by around 90 mb for all SCM simulations. One potential reason for this rapid growth is
695 the lack of a representation of detrainment into the RL in the SCM, as reflected by the
696 overestimation of the flux ratio, that would otherwise cool the CBL relative to the air above
697 and slow its growth (Figure 13d). During the growth phase of the CBL (up to around 1400
698 UTC) the flux ratios for the SCM mostly lie between 0.1 and 0.3, consistent with previous
699 studies of entrainment for boundary layers capped by strong inversions. For the LEM the
700 ratio is consistently less than 0.05 for the reasons discussed in section 3.2.3. Where the SCM
701 entrainment fluxes are weaker, especially when a longer timestep is used, this is not due to
702 a correct representation of PBL processes, but due to the difficulty in representing
703 entrainment with such weak inversions. The entrainment flux is parameterized through a
704 diffusion coefficient, calculated to give the desired flux from start-of-timestep fields (Lock *et*
705 *al.*, 2000). The flux ratio is systematically lower with a 15-minute timestep, then, because
706 reductions in the strength of the temperature inversion within the timestep lead to weaker
707 entrainment fluxes than the entrainment formula used might suggest. Weak entrainment
708 when using a 1-minute timestep, on the other hand, is mainly restricted to the period 1400
709 – 1430 UTC, and is due to the very low lapse rates directly above the temperature inversion
710 at this time. The rapid changes in the flux ratio in these simulations also highlight the
711 sensitivity of the SCM to small changes at the inversion as the CBL grows through the RL,
712 due to the weak stability there.

713 The SCM also struggles to reproduce the evolution of the vertical structure of the Saharan
714 ABL, with the potential temperature profile being too stable before 1400 UTC, and too
715 unstable afterwards (Figure 13a). The vertical structure is slightly improved with the shorter
716 timestep, making it more well mixed, which again suggests that the profile is evolving
717 rapidly relative to the timestep, leading to a temperature profile which is too diffuse.
718 Another shortcoming of the SCM is its failure to produce any cloud throughout the
719 simulation, because the mean relative humidity in the grid box never exceeds the critical
720 value of 80%. This is in contrast with the LEM, where clouds are formed in the areas where
721 the CBL is deepest. The SCM (and large-scale models more generally, given their coarse
722 horizontal resolution) do not represent the large CBL variability at scales of 5 – 10 km that is
723 observed, which provides the mechanism to bring parcels to their lifting condensation level.
724 Errors in cloud cover can have a large impact on the radiation budget, although more work
725 is needed to understand the relative importance of different forcings, such as clouds and
726 dust, on large-scale biases in the Sahara.
727 In summary, the SCM struggles to reproduce the typical 3-layer potential temperature
728 structure of the Saharan ABL, with a well-mixed CBL, weak inversion, and weakly-stable RL.
729 Due to the coarse vertical and temporal resolution, it cannot represent such a small
730 temperature inversion (in terms both of magnitude and vertical extent), and therefore
731 smooths the entire profile. CBL growth is faster compared to the LEM, suggesting that the
732 lack of a representation of detrainment in the SCM is having a significant impact. While
733 clouds are present in the LEM simulation, the SCM fails to trigger the cloud or convection
734 parameterisations at all. While here we provide a quick overview of potential problems in
735 the representation of the Saharan ABL in large-scale models given the insight provided by

736 the LEM results, a more in-depth analysis of these results will provide the basis for future
737 work.
738

739 # 4 Conclusions

740 A large-eddy simulation model and aircraft and radiosonde measurements made for the first
741 time in the remote Sahara have been used to describe the vertical structure and diurnal
742 evolution of the Saharan ABL. A schematic summarising the key features and processes
743 identified with both observations and the LEM is shown in Figure 14. The mean midday
744 Saharan ABL profile derived from radiosonde observations is characterized by a well-mixed
745 convective boundary layer capped by a small (<1 K) temperature inversion at approximately
746 820 mb, and a deep, near-neutral (lapse rate = 1 K Km^{-1}) residual layer which typically
747 reaches 550 mb. The large depth of the Saharan CBL produces a large variability in CBL
748 depths (up to 2km over short distances) and in the concentration of a passive tracer in the
749 LEM, despite the spatially homogeneous initial conditions and surface forcing; similar
750 variations were observed in CBL heights derived from the aircraft lidar. This large variability
751 in CBL properties solely due to turbulent processes means that caution must be used in the
752 interpretation of radiosonde profiles of the Saharan ABL, as any individual profile is unlikely
753 to be completely representative of the wider region. This sampling problem could
754 contribute to existing biases in analyses of the Saharan region, given the scarcity of
755 radiosondes being assimilated by operational systems. Turbulent processes can also
756 produce significant variability in boundary layer aerosol, such as dust, even in areas with
757 horizontally homogeneous emissions.
758 The mean properties of the CBL in the LEM agree closely with both radiosonde and aircraft
759 observations. While the strong surface heating leads to a broad distribution of vertical

760 velocities of −5 to 5 m s^{-1}, with peaks of 10 m s^{-1} at the CBL top, the potential temperatures
761 are confined to ±0.5 K of the CBL mean. In the RL, where the turbulent state is either
762 dominated by shear ($0 < Ri < 0.25$) or indeterminate ($0.25 < Ri < 1$), significant vertical
763 velocities are also measured (±2 m s^{-1}). These are due to a combination of externally-
764 imposed turbulence and waves from overshooting plumes, as well as shear-induced
765 turbulence at the RL top, which produce positive momentum fluxes and turbulent mixing
766 within the RL.
767 Despite the strong surface heating, and small capping inversion at the CBL top, entrainment
768 rates in the Saharan CBL are weak, leading to a slow CBL growth which does not erode the
769 RL completely until late afternoon in both the LEM and observations. A passive tracer
770 introduced in the CBL in the LEM simulation shows the presence of detrainment at the CBL
771 top. The temperature deficits of the warmest CBL plumes overshooting into the RL are very
772 small, which combined with the presence of some turbulence within the RL allows these
773 plumes to detrain from the CBL top. Detrainment reduces the entrainment rate via the
774 physical loss of material across the interface, and reduces the entrainment fluxes to only 3%
775 of the surface fluxes. As only the warmest plumes detrain, their negative heat flux
776 contribution is smaller than if they entrained RL air and returned to the CBL, and the
777 average CBL temperature is reduced, thus further slowing down the erosion of the
778 temperature inversion. As the CBL grows, detrained plumes can reach the RL top, where
779 they entrain free tropospheric air into the RL, thus producing a second entrainment zone at
780 the RL top. This second zone of entrainment warms the RL, helping maintain the
781 temperature inversion between the CBL and RL even longer and inhibiting CBL growth
782 further. These processes are particular to the Sahara, and possibly other deep, dry desert
783 boundary layers.

784 The Sahara is a major source of uncertainty in forecast models (Agusti-Panareda *et al.*, 2010,
785 Garcia-Carreras *et al.*, 2013). The particular structure of the Saharan ABL, and in particular
786 the small temperature inversion and deep near-neutral residual layer, directly impact its
787 dynamics and diurnal evolution. The Met Office Unified Model, run as an SCM driven by the
788 same data as the LEM simulation produces too rapid a boundary layer growth with no cloud
789 formation, highlighting the difficulties of large-scale models in representing key processes in
790 the Saharan ABL, due to their coarse vertical and time resolution. While here we present
791 only a quick overview of the SCM performance, a more detailed analysis of the process-
792 based representation of the Saharan ABL in large-scale models should be the focus of future
793 work. The model errors shown here have knock-on implications for the representation of a
794 number of important processes in the Sahara in numerical weather prediction models in
795 general. The influx of cool, moist air at low levels from the Atlantic to the west, and from
796 propagating cold pools in the north and south affects the large-scale structure of the
797 Saharan heat low (Todd *et al.*, 2013; Marsham *et al.*, 2013a and 2013b; Garcia-Carreras *et*
798 *al.*, 2013), and the Saharan ABL controls the vertical redistribution and long-term fate of this
799 moisture. The large depth of the Saharan ABL can lead to the formation of boundary layer
800 clouds despite the dry environment, and their radiative impact depends on the growth, and
801 final depth, of the CBL. Finally, the ability to explicitly simulate dust emissions depends on
802 the correct representation of near-surface gustiness, which depends on CBL turbulence and
803 the downward mixing of upper-level momentum, and dust radiative impacts are also
804 determined by its vertical, and subsequent long-range, transport. The additional impact of
805 mineral dust on boundary layer dynamics is not explored in this study, and should be
806 considered in future research.
807

Acknowledgements

Fennec was funded by a NERC consortium grant (NE/G017166/1). We would like to thank Azzedine Saci, Bouziane Ouchene, Mohammed Salah-Ferroudj, Benyakoub Abderrahmane, Mohammed Limam and Diali Sidali (ONM) for deploying and running the Fennec supersite and indeed all at ONM Algérie. Airborne data was obtained using the BAe-146-301 Atmospheric Research Aircraft operated by Directflight Ltd. and managed by FAAM, which is a joint entity of the NERC and the UK Met Office. The authors acknowledge the dedicated work of FAAM, Directflight and Avalon during the aircraft campaign.

817 **References**

818 Augusti-Panareda, A., A. Beljaars, C. Cardinali and I. Genkova, 2010: Impacts of
819 Assimilating AMMA Soundings on ECMWF Analyses and Forecasts, *Wea. Forecasting*, 25,
820 1142-1160.

821 Birch C. E., Parker D. J., Marsham J. H., Devine G. M., 2012: The effect of orography and
822 surface albedo on stratification in the summertime Saharan boundary layer: Dynamics and
823 implications for dust transport, *J. Geophys. Res.: Atmos.*, 117, doi: 10.1029/2011JD015965

824 Brooks I. M., Fowler A. M., 2007: New measure of entrainment zone structure, *Geophys.*
825 *Res. Lett.,* 34, doi: 10.1029/2007GL030958

826 Brooks I. M., Soderberg S., Tjernstrom M., 2003: The turbulence structure of the stable
827 atmospheric boundary layer around a coastal headland: Aircraft observations and modelling
828 results, *Bound.-Lay. Meteor.*, 107, pp.531-559.

829 Brown, A., R. Beare, J. Edwards, A. Lock, S. Keogh, S. Milton, and D. Walters, 2008:
830 Upgrades to the boundary layer scheme in the Met Office Numerical Weather Prediction
831 model. *Bound.-Layer Meteor.*, 128, 117 ï 132.

832 Canut, G., M. Lothon, F. Saïd, and F. Lohou, 2010: Observation of entrainment at the
833 interface between monsoon flow and the Saharan Air Layer, *Quarterly Journal of the Royal*
834 *Meteorological Society,* 136, 34 ï 46.

835 Conzemius, R. J., and E. Fedorovich, 2006: Dynamics of sheared convective boundary layer
836 entrainment. Part I: Methodological background and large-eddy simulations, *J. Atmos. Sci.*,
837 63, 1151 ï 1912.

838 Couvreux, F., F. Guichard, A. Gounou, D. Bouniol, P. Peyrillé and M. Köhler, 2014:
839 Modelling of the Thermodynamical Diurnal Cycle in the Lower Atmosphere: A Joint
840 Evaluation of Four Contrasted Regimes in the Tropics Over Land, *Boundary-Layer*
841 *Meteorol., 150*, 185 ï 214.

842

843 Cuesta, J., J. H. Marsham, D. J. Parker, C. Flamant, 2009: Dynamical mechanisms
844 controlling the vertical redistribution of dust and the thermodynamic structure of the West
845 Saharan Atmospheric Boundary Layer during Summer, *Atmos. Sci. Lett*., 10, 34-42, doi:
846 10.1002/asl.207.

847 Cuesta, J., D. Edouart, M. Mimouni, P.H. Flamant, C. Loth, F. Gibert, F. Marnas, A.
848 Bouklila, M. Kharef, B. Ouchene, M. Kadi and C. Flamant, 2008: Multiplatform observations
849 of the seasonal evolution of the Saharan atmospheric boundary layer in Tamanrasset, Algeria,
850 in the framework of the African Monsoon Multidisciplinary Analysis field campaign
851 conducted in 2006, *J. Geophys. Res*., 113, doi: 10.1029/2007JD009417.

852 Deardorff, J. W., G. E. Willis, and B. H. Stockton, 1980: Laboratory studies of the
853 entrainment zone of a convectively mixed layer, *J. Fluid Mech*., 100, 41 ï 64.

854 Fiedler, S., Schepanski, K., Heinold, B., Knippertz, P., and Tegen, I., 2013: Climatology of
855 nocturnal low-level Jets over North Africa and implications for simulating mineral dust
856 emission, *J. Geophys. Res.-Atmos.*, 118, 1-22, doi:10.1002/jgrd.50394.

857 Flamant, C., J. P. Chaboureau, D. J. Parker, C. A. Taylor, J. P. Cammas, O. Bock, F. Timouk and
858 J. Pelon, 2007: Airborne observations of the impact of a convective system on the planetary
859 boundary layer thermodynamics and aerosol distribution in the inter-tropical discontinuity
860 region of the West African Monsoon, *Quart. J. Roy. Meteorol. Soc*., 133, 1175-1189, doi:
861 10.1002/qj.97.

862 Fochesatto, G. J., P. Drobinski, C. Flamant, D. Guedalia, C. Sarrat, P. H. Flamant and J.
863 Pelon, 2001: Evidence of dynamical coupling between the residual layer and the developing
864 convective boundary layer, *Boundary-layer meteorology*, 99, 451-464.

865 Galperin, B., S. Sukoriansky and P. S. Anderson, 2007: On the critical Richardson number in
866 stably stratified turbulence, *Atmospheric Science Letters*, 8, 65-69.

867 Gamo, M., 1996: Thickness of the dry convection and large-scale subsidence above deserts.
868 *Bound.-Lay. Meteor.*, 79, 265ï 278.
869 Garcia-Carreras L, J. H. Marsham, D. J. Bain, S. Milton, A. Saci, M. Salah-Ferroudj, B.
870 Ouchene, R. Washington, 2013: The impact of convective cold pool outflows on model
871 biases in the Sahara, *Geophys. Res. Lett.*, 40*, 1647–1652, doi:10.1002/grl.50239.*
872 Gray, M. E. B., J. Petch, S. H. Derbyshire, A. R. Brown, A. P. Lock, H. A. Swann,
873 and P. R. A. Brown, 2001: Version 2.3 of the Met Office large eddy model, The Met. Office,
874 Exeter, UK.
875 Haywood, J., and O. Boucher, 2000: Estimates of the direct and indirect radiative forcing due
876 to tropospheric aerosols: A review, *Reviews of Geophysics*, 38(4), 513-543.
877 Huang, Q., J. H. Marsham, D. J. Parker, W. Tian and C. M. Grams, 2010: Simulations of the
878 effects of surface heat flux anomalies on stratification, convective growth and vertical
879 transport within the Saharan boundary layer, 115, doi:10.1029/2009JD012689.
880 Jickells, T. D., et al. (2005), Global iron connections between desert dust, ocean
881 biogeochemistry, and climate, *Science*, *308*(5718), 67-71.
882 Kaufman, Y. J., I. Koren, L. A. Remer, D. Rosenfeld, and Y. Rudich, 2005: The effect of
883 smoke, dust, and pollution aerosol on shallow cloud development over the Atlantic Ocean,
884 *Proc. Natl. Acad. Sci. U. S. A.*, 102(32), 11207-11212.
885 Lavaysse, C., C. Flamant, S. Janicot, D.J. Parker, J.P. Lafore, B. Sultan, J. Pelon, 2009:
886 Seasonal evolution of the West African heat low: a climatological perspective, *Climate*
887 *Dynamics*, 33, 3130330, doi: 10.1007/s00382-009-0553-4.
888 Lock, A. P., A. R. Brown, M. R. Bush, G. M. Martin and R. N. B. Smith, 2000: A new
889 boundary layer mixing scheme. Part I: Scheme description and single-column model tests.
890 *Monthly Weather Review*, 128(9), 3187-3199.

Lock, A. P., 2001: The numerical representation of entrainment in parametrizations of boundary layer turbulent mixing, *Monthly Weather Review*, 129, 1148ï 1163.

Marsham, J. H., M. Hobby, C. J. T. Allen, J. R. Banks, M. Bart, B. J. Brooks and R. Washington, 2013a: Meteorology and dust in the central Sahara: Observations from Fennec supersite-1 during the June 2011 Intensive Observation Period, *J. Geophys. Res. Atmos*., 118, 4069–4089, *doi:10.1002/jgrd.50211*.

Marsham, J. H., N. Dixon, L. Garcia-Carreras, G. M. S. Lister, D. J. Parker, P. Knippertz and C. Birch, 2013b: The role of moist convection in the West African monsoon system: Insights from continental-scale convection-permitting simulations, *Geophys. Res. Lett.*, 40, 1843ï 1849, doi:10.1002/grl.50347.

Marsham, J.H., D. J. Parker, C. M. Grams, B. T. Johnson, W. M. F. Grey and A. N. Ross, 2008: Observations of mesoscale and boundary-layer scale circulations affecting dust transport and uplift over the Sahara, *Atmos. Chem. Phys*., 8, 6979-6993.

Marsham, J.H., P. Knippertz, N. Dixon, D. J. Parker, G. M. S. Lister, 2011: The importance of the representation of deep convection for modeled dust-generating winds over West Africa during summer, *Geophys. Res. Lett*., 38, L16803, doi:10.1029/2011GL048368.

Matthews, A. J. and R. A. Madden, 2000: Observed propagation and structure of the 33-h atmospheric Kelvin wave, *J. Atmos. Sci.*, 57(21), 3488-3497.

Messager, C., D. Parker, O. Reitebuch, A. Agusti-Panareda, C. M. Taylor and J. Cuesta, 2010: Structure and dynamics of the Saharan atmospheric boundary layer during the West African monsoon onset: Observations and analyses from the research flights of 14 and 17 July 2006, *Q. J. Roy. Meteor. Soc.*, 107-124.

Moeng, C. H. and P. P. Sullivan, 1994: A comparison of shear and buoyancy driven planetary-boundary-layer flows, *J. Atmos. Sci.*, 51, 999 ï 1022.

915 Parker, D. J., R. R. Burton, A. Diongue-Niang, R. J. Ellis, M. Felton, C. M. Taylor, C. D.
916 Thorncroft, P. Bessemoulin and A. M. Tompkins, 2005: The diurnal cycle of the West
917 African monsoon circulation, *Q. J. Roy. Meteor. Soc.*, 131, 2839-2860, doi: 10.1256/qj.04.52.
918 Todd, M. C., et al., 2013: Meteorological and dust aerosol conditions over the western
919 Saharan region observed at Fennec Supersite-2 during the intensive observation period in
920 June 2011, *J. Geophys. Res. Atmos.*, 118, 8426ï 8447, doi:10.1002/jgrd.50470.
921 Pino, D., J. Vila-Guerau de Arellano and P. G. Duynkerke, 2003: The contribution of shear to
922 the evolution of a convective boundary layer, *J. Atmos. Sci.*, 60, 1913 ï 1926.
923 Prospero, J. M., P. Ginoux, O. Torres, S. E. Nicholson and T. E. Gill, 2002: Environmental
924 characterization of global sources of atmospheric soil dust identified with the Nimbus 7 Total
925 Ozone Mapping Spectrometer (TOMS) absorbing aerosol product, *Rev. Geophys.*, 40, doi:
926 10.1029/2000RG000095.
927 Roehrig, R., D. Bouniol, F. Guichard, F. Hourdin, and J.L. Redelsperger, 2013: The Present
928 and Future of the West African Monsoon: A Process-Oriented Assessment of CMIP5
929 Simulations along the AMMA Transect. *Journal of Climate, 26*(17).
930 Ryder, C. L., E. J. Highwood, P. D. Rosenberg, J. Trembath, J. K. Brooke, M. Bart, A. Dean,
931 J. Crosier, J. Dorsey, H. Brindley, J. Banks, J. H. Marsham, J. B. McQuaid, H. Sodemann,
932 and R. Washington, 2013: Optical properties of Saharan dust aerosol and contribution from
933 the coarse mode as measured during the Fennec 2011 aircraft campaign, *Atmos. Chem. Phys.*,
934 13, 303-325, doi:10.5194/acp-13-303-2013, 2013.
935 Stein, T. H. M., D. J. Parker, J. Delanoë, N. S. Dixon, R. J. Hogan, P. Knippertz, R. I.
936 Maidment and J. H. Marsham, 2011: The vertical cloud structure of the West African
937 monsoon: A 4 year climatology using CloudSat and CALIPSO, *J. Geophys. Res.*, 116,
938 D22205, doi:10.1029/2011JD016029.

939 Stull, R., 1988: An introduction to boundary layer meteorology, *Kluwer Academic*
940 *Publishers*, 175 ï 176.
941 Sullivan, P. P., C.-H. Moeng, B. Stevens, D. H. Lenschow and S. H. Mayor, 1998: Structure
942 of the entrainment zone capping the convective atmospheric boundary layer, *J. Atmos. Sci.*,
943 55, 3042 ï 3064.
944 Todd, M. C., et al., 2013: Meteorological and dust aerosol conditions over the western
945 Saharan region observed at Fennec Supersite-2 during the intensive observation period in
946 June 2011, *J. Geophys. Res.-Atmos.*, 118, doi:10.1002/jgrd.50470.
947 Walters, D. N., et al., 2014: The Met Office Unified Model Global Atmosphere 4.0 and
948 JULES Global Land 4.0 configurations, *Geosci. Model Dev.*, 7, 361-386, doi:10.5194/gmd-7-
949 361-2014.
950 Washington, R., M. Todd, N. J. Middleton and A. S. Goudie, 2003: Dust-storm source areas
951 determined by the total ozone monitoring spectrometer and surface observations, *Annals*
952 *Assoc. American. Geog.*, 93, 297-313, doi: 10.1111/1467-8306.9302003.
953 Washington, R., C. Flamant, D. J. Parker, J. H. Marsham, J. McQuaid, H. Brindley, M. Todd,
954 E. Highwood, C. Ryder, J-P. Chaboureau, C. Kocha, M. Bechir and A. Saci, 2012: Fennec -
955 The Saharan Climate System, *CLIVAR Exchanges*, No. 60, Vol. 17, No. 3, 31-32.
956 Weckwerth, Tammy M., James W. Wilson, Roger M. Wakimoto, 1996: Thermodynamic
957 Variability within the Convective Boundary Layer Due to Horizontal Convective Rolls. Mon.
958 Wea. Rev., 124, 769ï 784. doi: 10.1175/1520-0493.
959

Figure Captions

Figure 1: Met Office Unified Model analysis 925 mb potential temperature (colours) and mean sea-level pressure (white lines) averaged over June 2011. The 'L' indicates the approximate mean location of the Saharan heat low. The star shows the location of the radiosonde station at Bordj Badji Mokhtar, and the white straight line is the aircraft path.

Figure 2: All 1200 UTC radiosondes launched during 8 – 30 June 2011 (23 in total) normalized to each single CBL and RL top before averaging: (a) mean tephigram with wind barbs and (b) boxplot showing the 25th, 50th and 75th percentile of the gradient Richardson number in each layer.

Figure 3: Vertical profiles of potential temperature (solid lines) and water vapour mixing ratio (dashed lines) at 1200 UTC (black), 1500 UTC (red) and 1800 UTC (blue) in (a) BBM radiosondes launched on 20 June 2011 and (b) the LEM simulation. The horizontal dotted lines show the CBL and RL top heights at 1200 UTC.

Figure 4: Contours of a passive tracer initialized at 0900 UTC in the lowest model level (left) and vertical velocity (right) at 1300, 1400, 1500 and 1600 UTC (top to bottom). Red contour lines filled in white show clouds.

Figure 5: Vertical velocity (solid line) and potential temperature (dotted line) at 1510 UTC for a single plume measured by the aircraft at -5.04E, 23.89N and 620 mb.

Figure 6: Probability density function of potential temperature anomaly and vertical velocity in the RL (a, b) and CBL (c, d) in the LEM (1400 UTC, black), the BBM radiosondes (1200 UTC, red) and the aircraft observations (1400 – 1500 UTC, blue).

Figure 7: Normalized momentum (dashed black line), sensible heat (red line) and humidity (blue line) fluxes in the LEM simulation and domain-mean potential temperature (solid black

983 line) at (a) 1200 UTC, (b) 1300 UTC, (c) 1400 UTC, (d) 1500 UTC and (e) 1600 UTC. The
984 humidity fluxes were normalized using the maximum in the absolute value of the flux.
985 Figure 8: 1300 UTC LEM potential temperature perturbation from the horizontal mean (left)
986 and vertical velocity (right), with horizontal wind vectors, at 630 mb.
987 Figure 9: (a) 1400 UTC LEM potential temperature anomaly from the horizontal mean
988 (colour contours) and vertical velocity (−0.5 m s-1 and 0.5 m s-1 for the black dashed and
989 solid black lines respectively) at 630 mb, and tracer concentrations at 665 mb (thick, purple
990 contours). The different heights are used to highlight the impact of plumes (shown by the
991 tracer concentrations) on the air directly above. (b) same as (a) but along an x-z transect
992 perpendicular to the wave pattern (dotted line in panel a), with wind vectors overplotted
993 (vertical velocity contours are omitted).
994 Figure 10: Aircraft track contoured with virtual potential temperature. The track shown
995 extends from -5.4E, 24.0N (x = 0km) to -4.4E, 23.7N (see also the white line in Figure 1).
996 Measurements cover the period from 1352 UTC (start of the lowest leg) to 1514 UTC (end of
997 the uppermost leg). The potential temperature profiles from the two dropsondes launched
998 before the descent (at 1313 and 1320 UTC) are overplotted in black, with the vertical dotted
999 lines indicating their location. The dashed line shows the CBL height as derived from the on-
1000 board Lidar. The vertical dash-dot line shows the boundary for the ‘east’ and ‘west’ portions
1001 used in the analysis.
1002 Figure 11: (a,b) Aircraft observations of vertical velocity (blue line), potential temperature
1003 (red line) and the product of the vertical velocity and potential temperature perturbations
1004 (black line) at (a) 680 mb and (b) 620 mb. Anomalies were computed as deviations from the
1005 timeseries with a 10 km high-pass filter applied. (c,d) Coherency-squared as a function of
1006 length scale for potential temperature and vertical velocity at 680 mb (solid line) and 620

1007 mb (dashed line) for data where (c) x < 60 km (West of -4.85°E) and (d) x > 60 km (East of -
1008 4.85°E). The horizontal solid line indicates the 95% significance level. The insets show the
1009 phase functions for these pairs of measurements.
1010 Figure 12: (a) Sensible heat fluxes and (b) momentum fluxes calculated using the eddy
1011 covariance method for each level leg of the aircraft case, split between the western
1012 (crosses) and eastern (stars) sections of the track, and using the descent into the study area
1013 (solid line) and ascent away from the study area (dotted line). The boundary for the 'East'
1014 and 'West' portions was at -4.85E.
1015 Figure 13: (a) Potential temperature in the Unified Model SCM using a 15-minute timestep
1016 (solid line) and a 1-minute timestep (dashed line) and in the LEM (dotted line) and (b)
1017 potential temperature in the SCM with a 1-minute timestep and 62 (solid), 70 (dashed) and
1018 140 (dotted) vertical levels at 1200 UTC (black), 1400 UTC (red), and 1600 UTC (blue). (c)
1019 Boundary layer height and (d) flux ratio in the 5 simulations.
1020 Figure 14: Schematic describing the main features of the Saharan ABL and the fate of
1021 overshooting parcels as the CBL grows. The bell-shape curve describes the distribution of
1022 temperatures in the CBL, and the dashed lines show the fate of plumes of different
1023 temperatures as follows: 1. Cooler CBL plumes entrain RL air into the CBL, contributing to
1024 CBL warming and growth. 2. Warmer CBL plumes are detrained, as their temperature is
1025 similar to the RL and mixing within the RL from shear contributes to mixing them out. This
1026 cools the CBL and slows down CBL growth. 3. As the CBL grows, some plumes reach the RL
1027 top, entraining free-tropospheric air into the RL. This schematic provides a 1D view of the
1028 key processes occurring within the Saharan ABL. In reality, turbulent processes also produce
1029 a horizontal variability in CBL depths of up to 50% of the total over horizontal distances of
1030 the order of the CBL height.

Figures

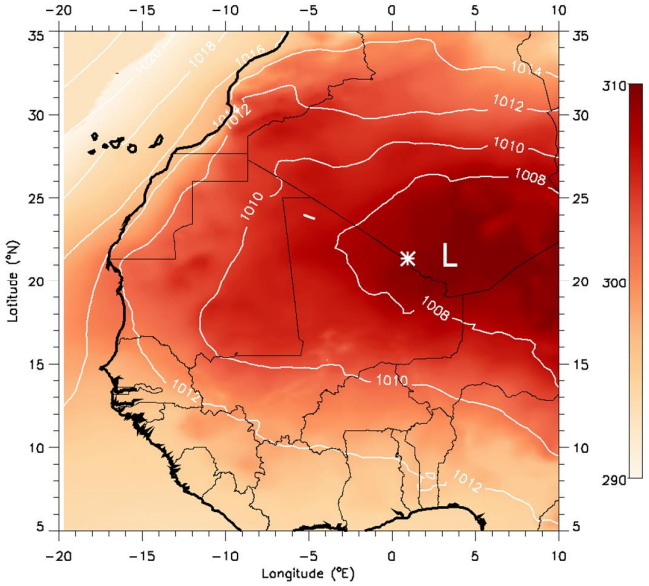

Figure 1: Met Office Unified Model analysis 925 mb potential temperature (colours) and mean sea-level pressure (white lines) averaged over June 2011. The 'L' indicates the approximate mean location of the Saharan heat low. The star shows the location of the radiosonde station at Bordj Badji Mokhtar, and the white straight line is the aircraft path.

1038

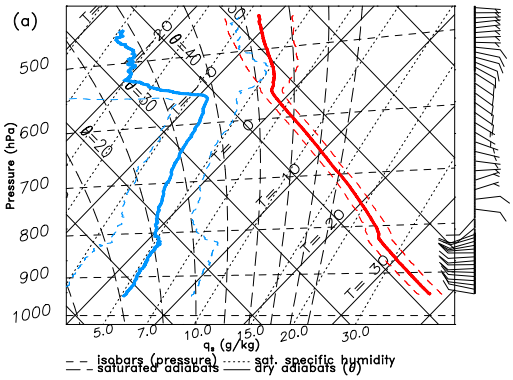

1039

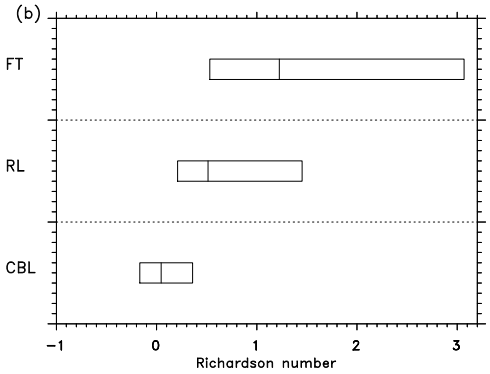

1040

1041

1042 **Figure 2:** All 1200 UTC radiosondes launched during 8 – 30 June 2011 (23 in total)

1043 normalized to each single CBL and RL top before averaging: (a) mean tephigram with wind

1044 barbs and (b) boxplot showing the 25th, 50th and 75th percentile of the gradient Richardson

1045 number in each layer.

1046

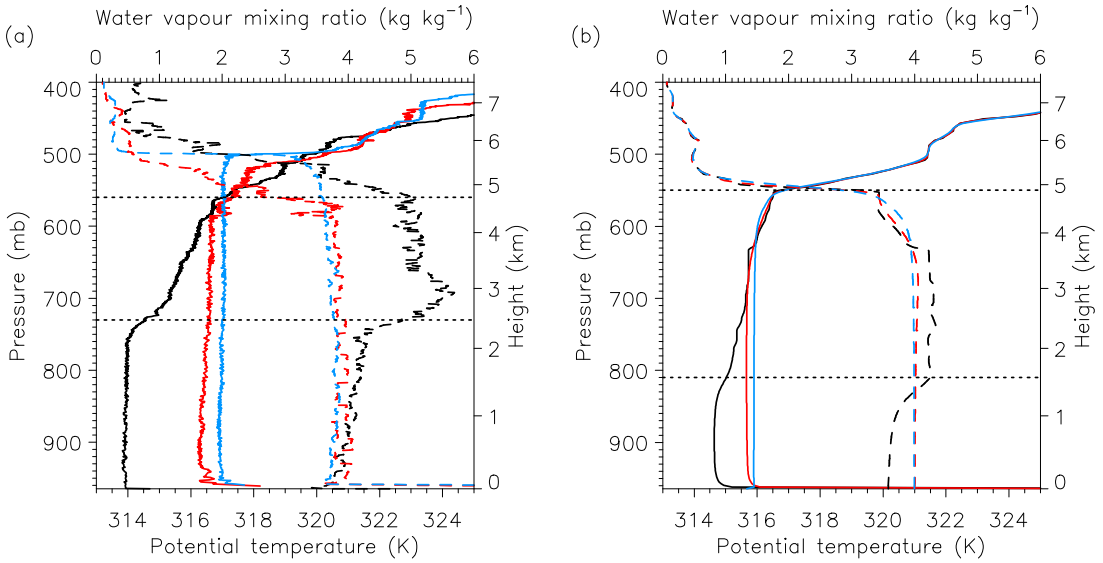

1047

1048 **Figure 3:** Vertical profiles of potential temperature (solid lines) and water vapour mixing

1049 ratio (dashed lines) at 1200 UTC (black), 1500 UTC (red) and 1800 UTC (blue) in (a) BBM

1050 radiosondes launched on 20 June 2011 and (b) the LEM simulation. The horizontal dotted

1051 lines show the CBL and RL top heights at 1200 UTC.

1052

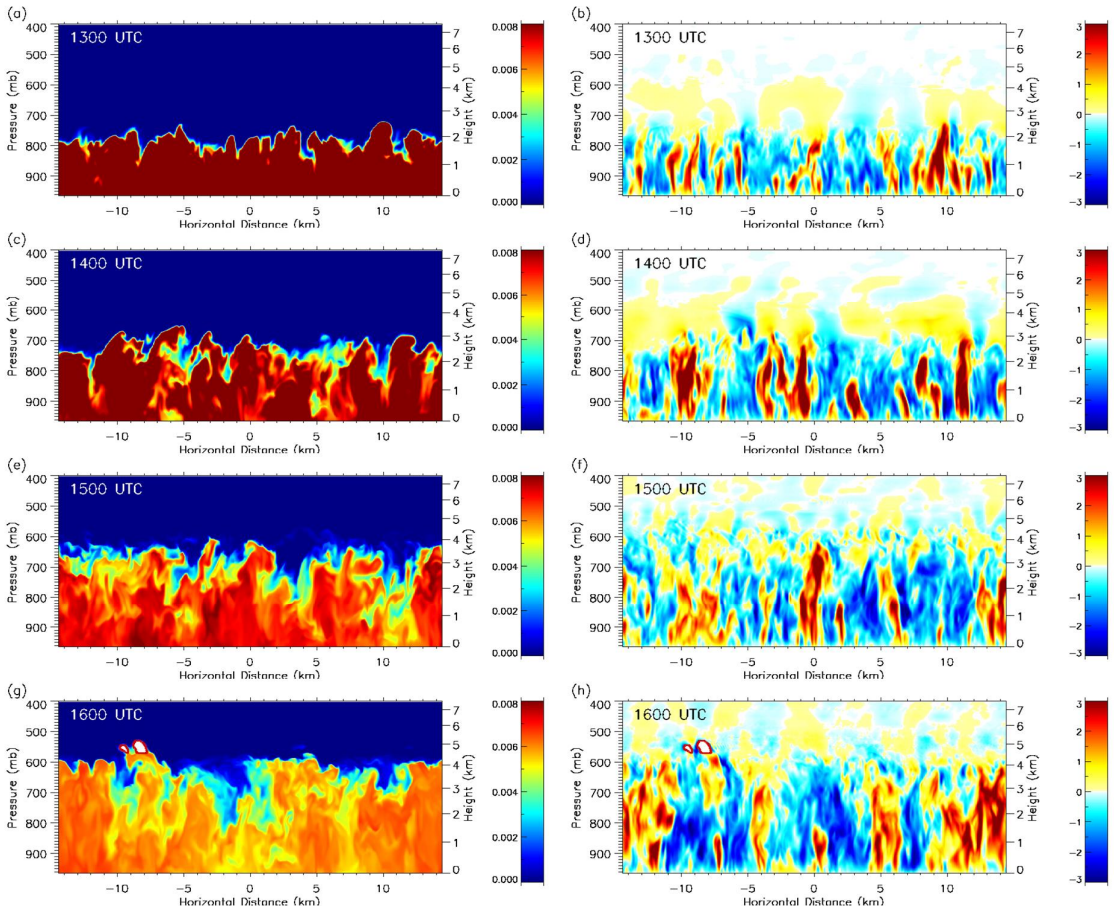

1053

1054 **Figure 4:** Contours of a passive tracer initialized at 0900 UTC in the lowest model level (left)

1055 and vertical velocity (right) at 1300, 1400, 1500 and 1600 UTC (top to bottom). Red contour

1056 lines filled in white show clouds.

1057

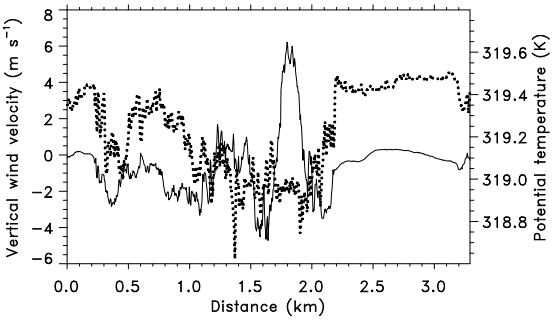

1058

1059 **Figure 5:** Vertical velocity (solid line) and potential temperature (dotted line) at 1510 UTC

1060 for a single plume measured by the aircraft at -5.04E, 23.89N and 620 mb.

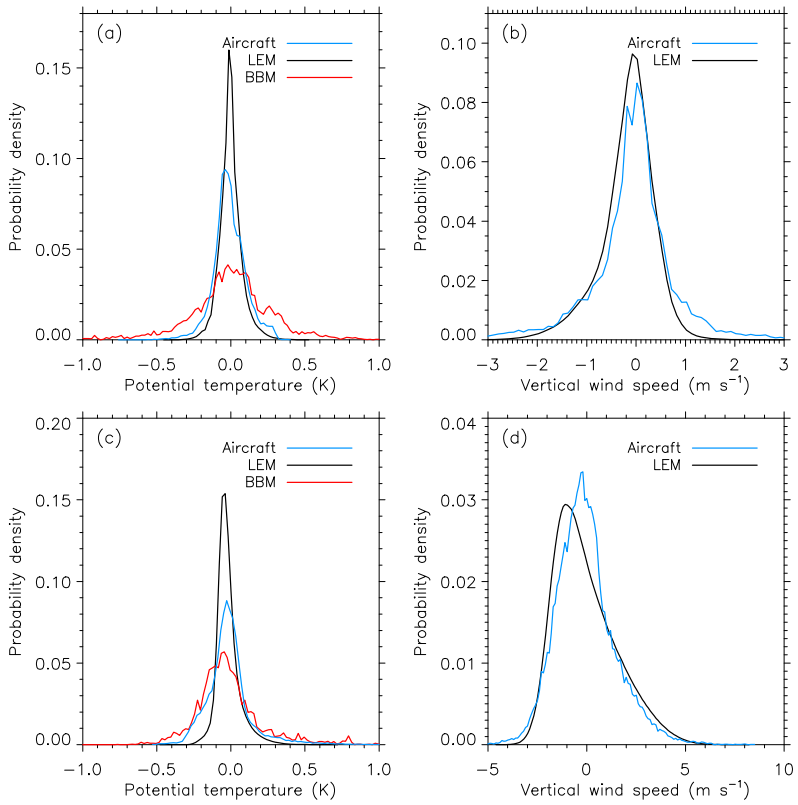

Figure 6: Probability density function of potential temperature anomaly and vertical velocity in the RL (a, b) and CBL (c, d) in the LEM (1400 UTC, black), the BBM radiosondes (1200 UTC, red) and the aircraft observations (1400 – 1500 UTC, blue).

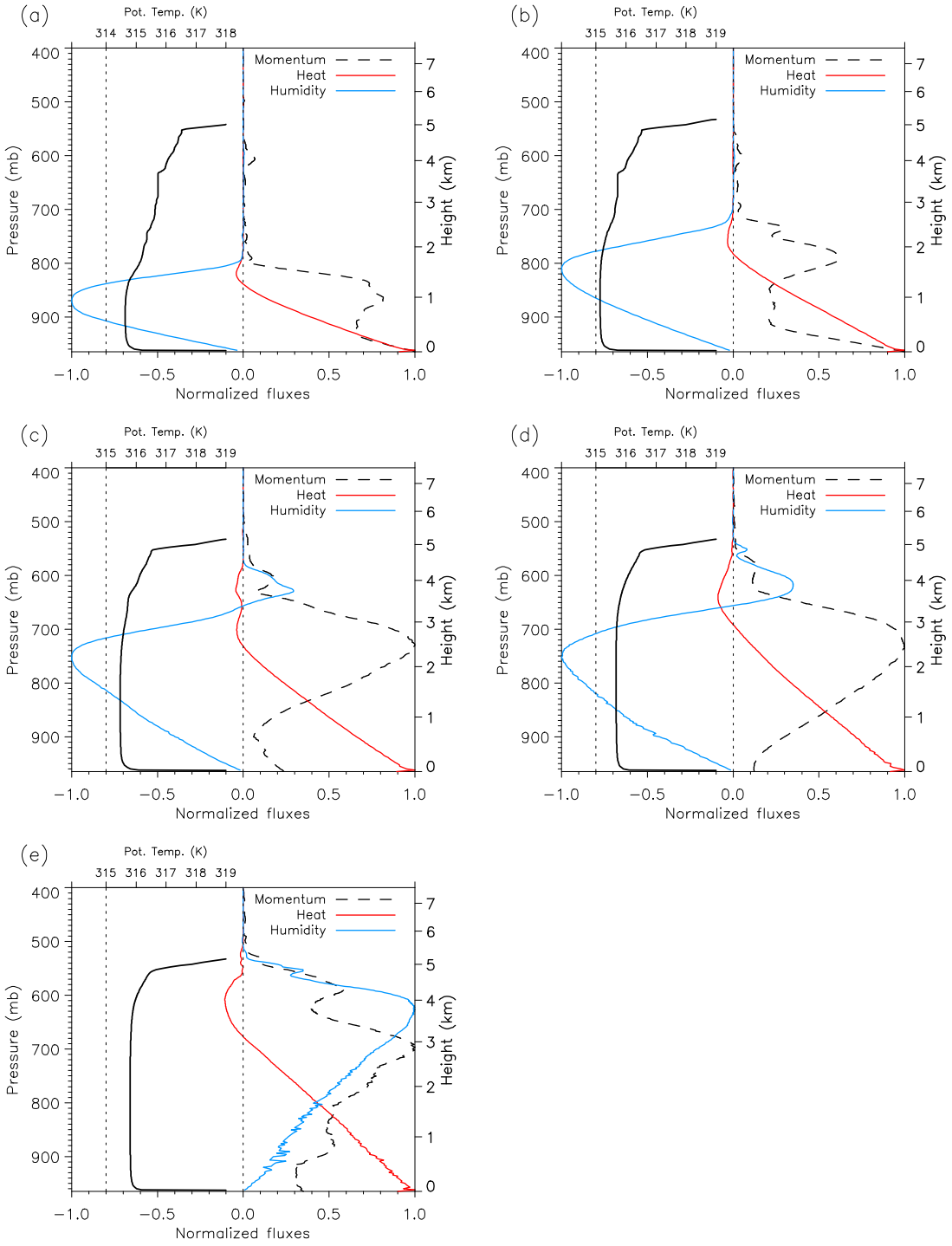

Figure 7: Normalized momentum (dashed black line), sensible heat (red line) and humidity (blue line) fluxes in the LEM simulation and domain-mean potential temperature (solid black line) at (a) 1200 UTC, (b) 1300 UTC, (c) 1400 UTC, (d) 1500 UTC and (e) 1600 UTC. The humidity fluxes were normalized using the maximum in the absolute value of the flux.

1073

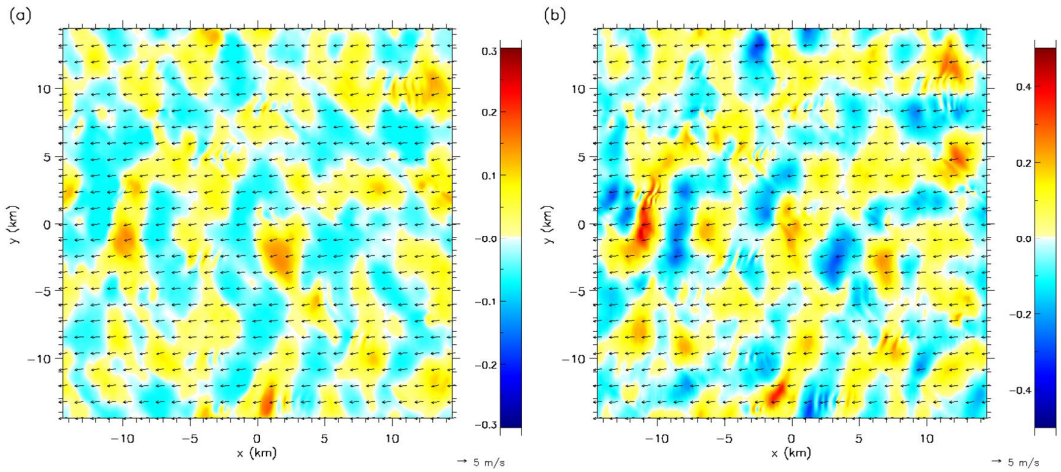

1074

1075 **Figure 8:** 1300 UTC LEM potential temperature perturbation from the horizontal mean (left)

1076 and vertical velocity (right), with horizontal wind vectors, at 630 mb.

1077

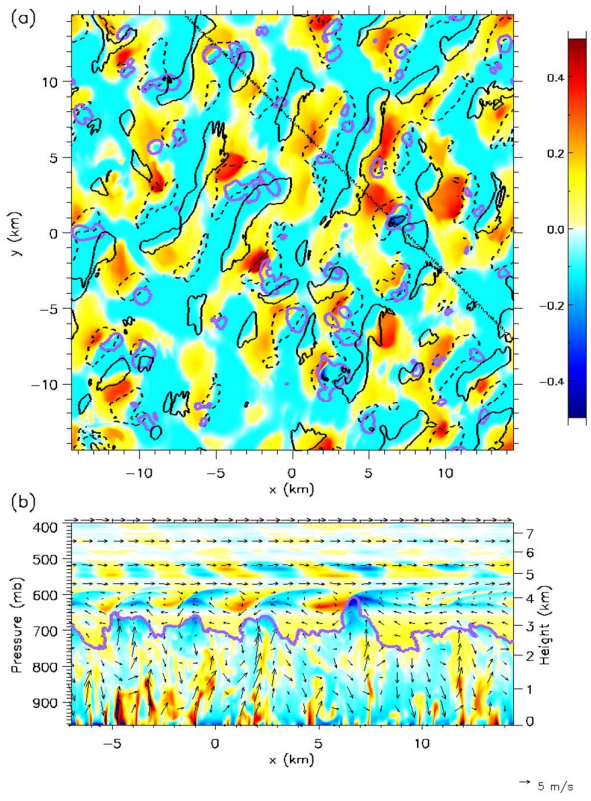

1078

Figure 9: (a) 1400 UTC LEM potential temperature anomaly from the horizontal mean (colour contours) and vertical velocity (–0.5 m s^{-1} and 0.5 m s^{-1} for the black dashed and solid black lines respectively) at 630 mb, and tracer concentrations at 665 mb (thick, purple contours). The different heights are used to highlight the impact of plumes (shown by the tracer concentrations) on the air directly above. (b) same as (a) but along an x-z transect perpendicular to the wave pattern (dotted line in panel a), with wind vectors overplotted (vertical velocity contours are omitted).

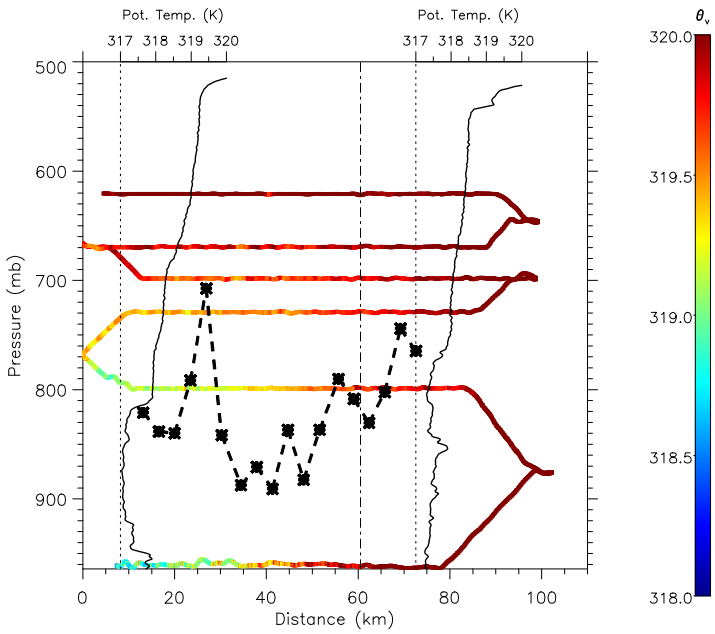

Figure 10: Aircraft track contoured with virtual potential temperature. The track shown extends from -5.4E, 24.0N (x = 0km) to -4.4E, 23.7N (see also the white line in Figure 1). Measurements cover the period from 1352 UTC (start of the lowest leg) to 1514 UTC (end of the uppermost leg). The potential temperature profiles from the two dropsondes launched before the descent (at 1313 and 1320 UTC) are overplotted in black, with the vertical dotted lines indicating their location. The dashed line shows the CBL height as derived from the on-

board Lidar. The vertical dash-dot line shows the boundary for the 'east' and 'west' portions used in the analysis.

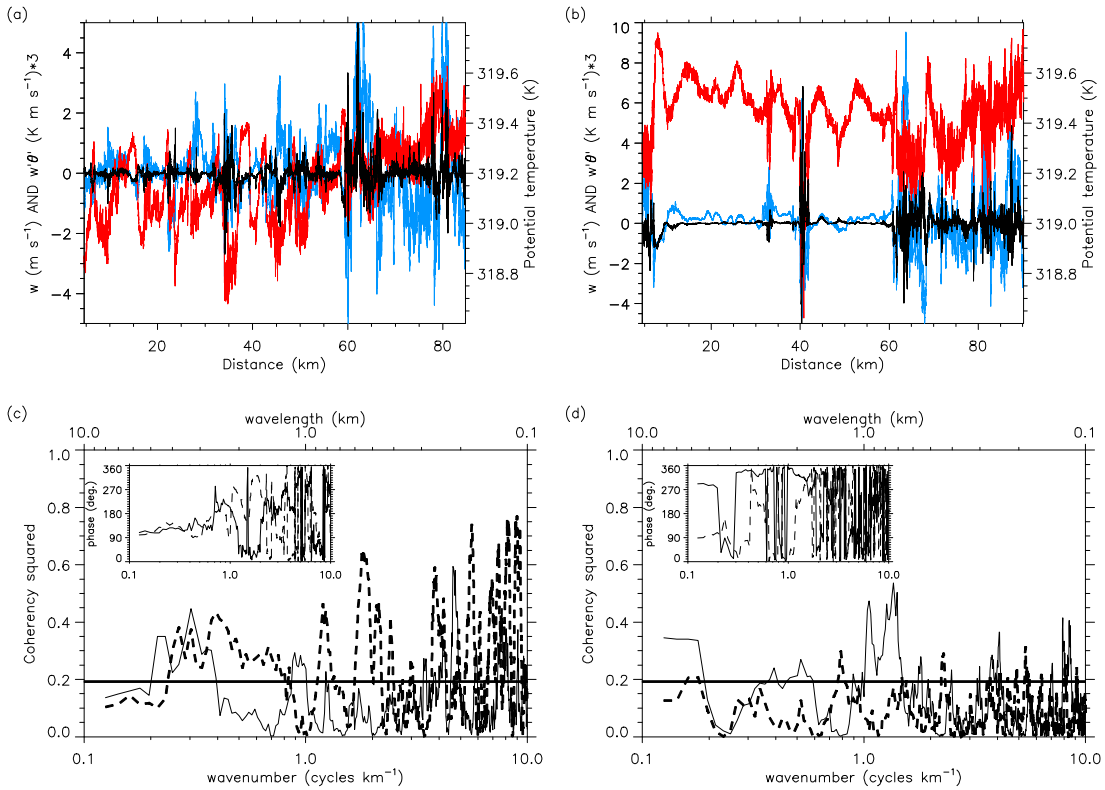

Figure 11: (a,b) Aircraft observations of vertical velocity (blue line), potential temperature (red line) and the product of the vertical velocity and potential temperature perturbations (black line) at (a) 680 mb and (b) 620 mb. Anomalies were computed as deviations from the timeseries with a 10 km high-pass filter applied. (c,d) Coherency-squared as a function of length scale for potential temperature and vertical velocity at 680 mb (solid line) and 620 mb (dashed line) for data where (c) x < 60 km (West of -4.85°E) and (d) x > 60 km (East of -4.85°E). The horizontal solid line indicates the 95% significance level. The insets show the phase functions for these pairs of measurements.

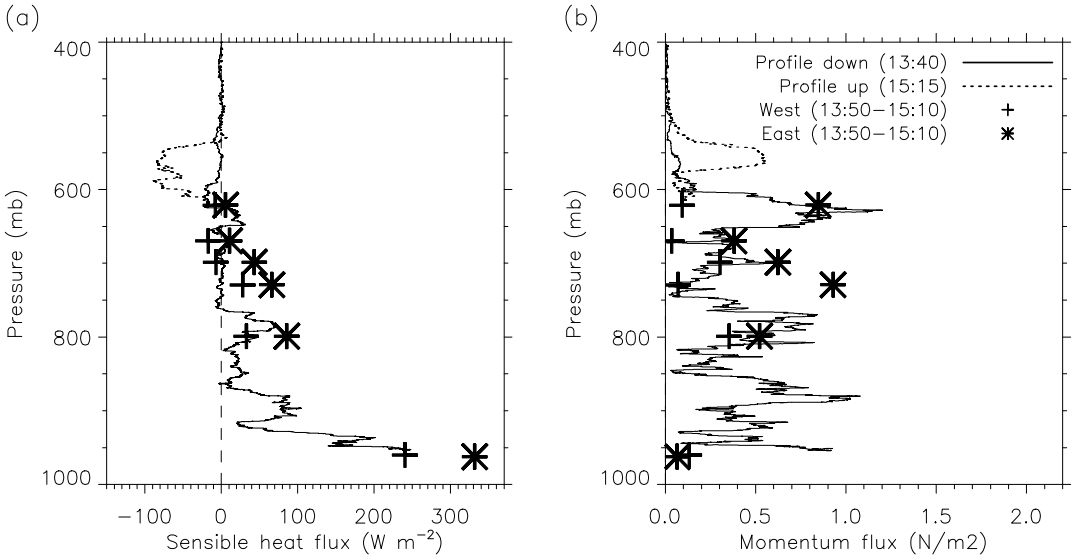

1107

1108 **Figure 12:** (a) Sensible heat fluxes and (b) momentum fluxes calculated using the eddy
1109 covariance method for each level leg of the aircraft case, split between the western
1110 (crosses) and eastern (stars) sections of the track, and using the descent into the study area
1111 (solid line) and ascent away from the study area (dotted line). The boundary for the 'East'
1112 and 'West' portions was at -4.85E.

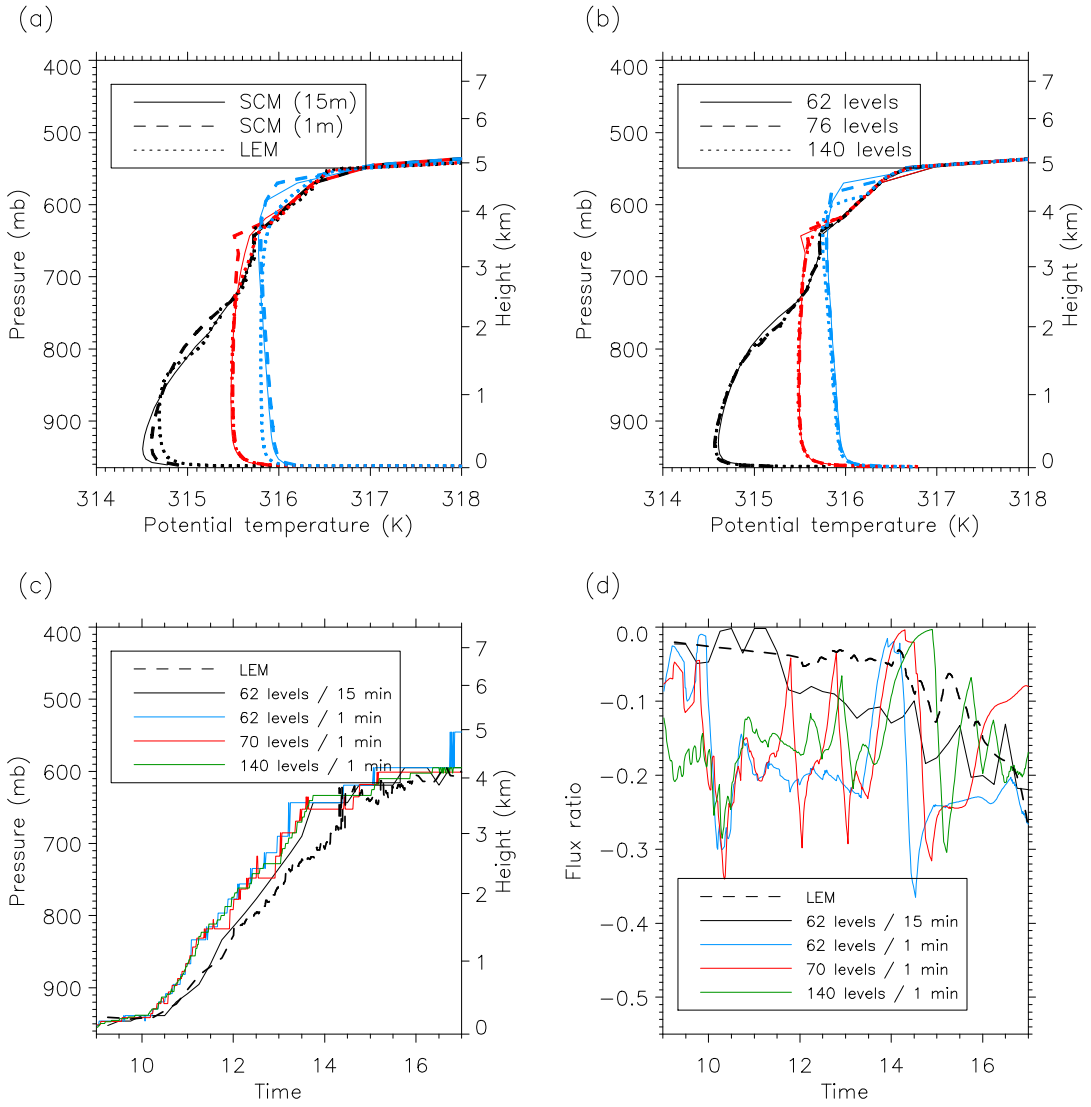

Figure 13: (a) Potential temperature in the Unified Model SCM using a 15-minute timestep (solid line) and a 1-minute timestep (dashed line) and in the LEM (dotted line) and (b) potential temperature in the SCM with a 1-minute timestep and 62 (solid), 70 (dashed) and 140 (dotted) vertical levels at 1200 UTC (black), 1400 UTC (red), and 1600 UTC (blue). (c) Boundary layer height and (d) flux ratio in the 5 simulations.

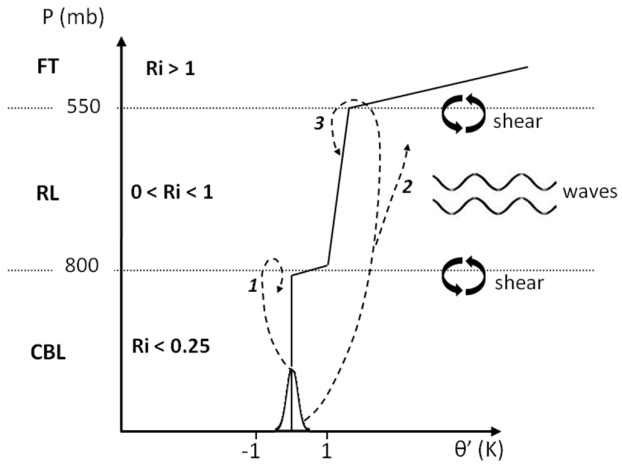

Figure 14: Schematic describing the main features of the Saharan ABL and the fate of overshooting parcels as the CBL grows. The bell-shape curve describes the distribution of temperatures in the CBL, and the dashed lines show the fate of plumes of different temperatures as follows: 1. Cooler CBL plumes entrain RL air into the CBL, contributing to CBL warming and growth. 2. Warmer CBL plumes are detrained, as their temperature is similar to the RL and mixing within the RL from shear contributes to mixing them out. This cools the CBL and slows down CBL growth. 3. As the CBL grows, some plumes reach the RL top, entraining free-tropospheric air into the RL. This schematic provides a 1D view of the key processes occurring within the Saharan ABL. In reality, turbulent processes also produce a horizontal variability in CBL depths of up to 50% of the total over horizontal distances of the order of the CBL height.